

# The Outer Solar System Origins Survey: I. Design and First-Quarter Discoveries

Michele T. Bannister<sup>1,2</sup>, J. J. Kavelaars<sup>1,2</sup>, Jean-Marc Petit<sup>3</sup>, Brett J. Gladman<sup>4</sup>, Stephen D. J. Gwyn<sup>2</sup>, Ying-Tung Chen<sup>5</sup>, Kathryn Volk<sup>6</sup>, Mike Alexandersen<sup>4,5</sup>, Susan Benecchi<sup>7</sup>, Audrey Delsanti<sup>8</sup>, Wesley Fraser<sup>2,9</sup>, Mikael Granvik<sup>10,11</sup>, Will M. Grundy<sup>12</sup>, Aurélie Guilbert-Lepoutre<sup>3</sup>, Daniel Hestroffer<sup>13</sup>, Wing-Huen Ip<sup>14,15</sup>, Marian Jakubik<sup>16</sup>, Lynne Jones<sup>17</sup>, Nathan Kaib<sup>18</sup>, Pedro Lacerda<sup>19</sup>, Samantha Lawler<sup>2</sup>, Matthew J. Lehner<sup>5,20,21</sup>, Hsing Wen Lin<sup>14</sup>, Tim Lister<sup>22</sup>, Patryk Sofia Lykawka<sup>23</sup>, Stephanie Monty<sup>1</sup>, Michael Marsset<sup>8,24</sup>, Ruth Murray-Clay<sup>25</sup>, Keith Noll<sup>26</sup>, Alex Parker<sup>27</sup>, Rosemary E. Pike<sup>1</sup>, Philippe Rousset<sup>3</sup>, David Rusk<sup>1</sup>, Megan E. Schwamb<sup>5</sup>, Cory Shankman<sup>1</sup>, Bruno Sicardy<sup>28</sup>, Pierre Vernazza<sup>8</sup>, Shiang-Yu Wang<sup>5</sup>

micheleb@uvic.ca

---

<sup>1</sup>Department of Physics and Astronomy, University of Victoria, Elliott Building, 3800 Finnerty Rd, Victoria, BC V8P 5C2, Canada

<sup>2</sup>NRC-Herzberg Astronomy and Astrophysics, National Research Council of Canada, 5071 West Saanich Rd, Victoria, British Columbia V9E 2E7, Canada

<sup>3</sup>Institut UTINAM UMR6213, CNRS, Univ. Bourgogne Franche-Comté, OSU Theta F25000 Besançon, France

<sup>4</sup>Department of Physics and Astronomy, University of British Columbia, Vancouver, BC, Canada

<sup>5</sup>Institute for Astronomy and Astrophysics, Academia Sinica; 11F AS/NTU, National Taiwan University, 1 Roosevelt Rd., Sec. 4, Taipei 10617, Taiwan

<sup>6</sup>Department of Planetary Sciences/Lunar and Planetary Laboratory, University of Arizona, 1629 E University Blvd, Tucson, AZ 85721, United States

<sup>7</sup>Planetary Science Institute, 1700 East Fort Lowell, Suite 106, Tucson, AZ 85719, United States

<sup>8</sup>Aix Marseille Université, CNRS, LAM (Laboratoire d’Astrophysique de Marseille) UMR 7326, 13388, Marseille, France

<sup>9</sup>Queen’s University Belfast, Astrophysics Research Centre, Belfast, Northern Ireland

<sup>10</sup>Department of Physics, P.O. Box 64, 00014 University of Helsinki, Finland

<sup>11</sup>Finnish Geospatial Research Institute, P.O. Box 15, 02430 Masala, Finland

<sup>12</sup>Lowell Observatory, Flagstaff, Arizona, United States

<sup>13</sup>IMCCE, Observatoire de Paris - PSL research univ., UPMC univ. P06, univ. Lille 1, CNRS, F-75014 Paris, France

<sup>14</sup>Institute of Astronomy, National Central University, Taiwan

<sup>15</sup>Space Science Institute, Macau University of Science and Technology, Macau

<sup>16</sup>Astronomical Institute, Slovak Academy of Science, 05960 Tatranska Lomnica, Slovakia

<sup>17</sup>University of Washington, Washington, United States

<sup>18</sup>HL Dodge Department of Physics & Astronomy, University of Oklahoma, Norman, OK 73019, United States

<sup>19</sup>Max Planck Institute for Solar System Research, Justus-von-Liebig-Weg 3, 37077 Göttingen, Germany

<sup>20</sup>Department of Physics and Astronomy, University of Pennsylvania, 209 S. 33rd St., Philadelphia, PA 19104, USA

<sup>21</sup>Harvard-Smithsonian Center for Astrophysics, 60 Garden St., Cambridge, MA 02138, USA

<sup>22</sup>Las Cumbres Observatory Global Telescope Network, Inc., 6740 Cortona Drive Suite 102, Goleta, CA 93117, United States

<sup>23</sup>Astronomy Group, School of Interdisciplinary Social and Human Sciences, Kinki University, Japan

## ABSTRACT

We report 85 trans-Neptunian objects (TNOs) from the first 42 deg<sup>2</sup> of the Outer Solar System Origins Survey (OSSOS), an ongoing  $r$ -band survey with the 0.9 deg<sup>2</sup> field-of-view MegaPrime camera on the 3.6 m Canada-France-Hawaii Telescope. A dense observing cadence and our innovative astrometric technique produced survey-measured orbital elements for these TNOs precise to a fractional semi-major axis uncertainty  $< 0.1\%$  in two sequential years, instead of the 3–5 years needed with sparser observing strategies. These discoveries are free of ephemeris bias, a first for large Kuiper belt surveys. The survey’s simulator provides full characterization, including calibrated detection efficiency functions, for debiasing the discovery sample. We confirm the existence of a cold “kernel” of objects within the main cold classical Kuiper belt, and imply the existence of an extension of the “stirred” cold classical Kuiper belt to at least several AU beyond the 2:1 mean motion resonance with Neptune. The population model of Petit et al. (2011) remains a plausible interpretation of the Kuiper belt. The full survey will provide an exquisitely characterized sample of important resonant TNO populations, ideal for testing models of giant planet migration during the early history of the Solar System.

*Subject headings:* Kuiper belt: general — surveys

## 1. Introduction

We present here the design and initial observations and discoveries of the Outer Solar System Origins Survey (OSSOS). OSSOS will provide a flux-limited sample of approximately five hundred trans-Neptunian objects (TNOs), with high-precision, dynamically classified orbits. The survey is especially sensitive to TNOs that are in exterior mean-motion resonance with Neptune. OSSOS will measure the absolute abundance and internal orbital distributions

---

<sup>24</sup>European Southern Observatory (ESO), Alonso de Córdova 3107, 1900 Casilla Vitacura, Santiago, Chile

<sup>25</sup>Department of Physics, University of California, Santa Barbara, CA 93106, USA

<sup>26</sup>NASA Goddard Space Flight Center, Code 693, Greenbelt, MD 20771, United States

<sup>27</sup>Southwest Research Institute, Boulder, Colorado, United States

<sup>28</sup>LESIA, Observatoire de Paris, CNRS UMR 8109, Université Pierre et Marie Curie, Université Paris-Diderot, 5 place Jules Janssen, F-92195 Meudon Cedex, France

of numerous resonant populations, the main classical belt, the scattering and detached populations, and the libration amplitude distribution in many low-order resonances. The OSSOS dataset will provide direct constraints for cosmogonic scenarios that consistently explain all observed features of the trans-Neptunian populations.

The populations of TNOs are not in a flat, circular disk. Discerning the features of the populations has required many sky surveys; (Bannister in press, 2015, reviews these). The present TNO orbital distribution is a signature of excitation events that occurred earlier in the dynamical history of the Solar System (Fernandez & Ip 1984). Certain features of the orbital distribution are diagnostic of the evolutionary processes that sculpted the disk. Foremost among these features are the TNOs trapped in the mean-motion resonances with Neptune. The population abundances and orbital distribution in each mean-motion resonance with Neptune are dependent on the mechanism that emplaced the dynamically excited Kuiper belt. Were resonant TNOs trapped from pre-existing low-eccentricity orbits, then pumped to higher eccentricities during subsequent migration (e.g. Malhotra 1995; Hahn & Malhotra 1999, 2005), or were they trapped into the resonances out of a scattering population, after which their eccentricities were damped (e.g. Levison et al. 2008; Nesvorny 2015)? For one example of how resonant TNOs can test planet migration, the distribution of TNOs within the substructure of the 2:1 resonance places limits on Neptune’s migration history: the speed of its past migration influences the present ratio of objects leading or trailing Neptune in orbital longitude (Murray-Clay & Chiang 2005). Because the asymmetry appears to be small, the discovery of more TNOs that orbit within these diagnostic features is required (e.g. Murray-Clay & Chiang 2005; Gladman et al. 2012). The OSSOS dataset will enable testing of the veracity of proposed models of initial radial planetesimal distribution, planet migration distances and time scales. The OSSOS survey simulator will allow the comparison of the observed trans-Neptunian population to model outputs.

OSSOS is designed to discover the necessary new sample of TNOs in a way that allows the underlying populations’ orbit distribution to be determined. TNO discovery is inherently prone to observationally induced biases (Trujillo 2000; Jones et al. 2006; Kavelaars et al. 2008; Jones et al. 2010). For example, the 5:1 resonance has such a large semi-major axis (88 au) that a typical object in the 5:1 would only be visible in a flux-limited sample for  $< 1\%$  of its orbital period (Gladman et al. 2012). Minimal loss of objects following their discovery, and accurate survey debiasing, are necessary to ascertain the population structure of these hard-to-sample resonances.

Drawing on the experiences of well-calibrated wide-field surveys like the Canada-France Ecliptic Plane Survey (CFEPS) (Jones et al. 2006; Kavelaars et al. 2009; Petit et al. 2011), Alexandersen et al. (2014), and the Deep Ecliptic Survey (Elliot et al. 2005; Millis et al.

2002), we aim to acquire a TNO sample free of *ephemeris bias* (Jones et al. 2006): selection effects from the choices of orbit estimation and of recovery observations. OSSOS is conducted as a queue-mode Large Program with the MegaCam imager on the 3.6 m Canada-France-Hawaii Telescope (CFHT) to discover and to follow-up our discoveries. Follow-up is  $> 90\%$  of the survey’s 560-hour time budget, and allows us to constrain the orbits of our discoveries with exquisite precision. This removes the need for follow-up to confirm orbits by facilities other than the survey telescope. Objects are tracked until their orbital classification (§ 6.4) is secure, which at minimum requires reaching semi-major axis uncertainties  $\sigma_a < 1\%$ , and which may require reaching  $\sigma_a < 0.01\%$ .

We describe here our observation strategy, our astrometric and photometric calibration, the open-source data processing pipeline, the characterization of our TNO detection efficiency, the survey’s simulator, and the discoveries in the first quarter of the survey.

## 2. Survey design and observations

The OSSOS observations are acquired in *blocks*: contiguous patches of sky formed by a layout of adjoining multiple MegaCam fields. These are made large enough to reduce the chance of losing objects due to orbit shear, and sufficiently narrow in right ascension to be easily queue-scheduled for multiple observations in a single night. For the discovery blocks reported here (§ 2.3), a 3 x 7 grid of pointings was used to achieve this goal (Fig. 1).

The survey is observed in two parts, as a given right ascension can only be observed for  $\sim 6$  months at a time. During the discovery opposition, a block is observed multiple times in each of five to six lunations to provide robust determination of discovered object orbits. Field centers shift during this time by drifting the block over the six months at the Kuiper belt average sky motion rate, which tracks the TNOs present in that area of sky (§ 2.2). A year later, the next opposition is dedicated to discovery followup (§ 2.2). The orbit determination from the first year is good enough to allow pointed recoveries of each object during the second year (§ 6.1).

The survey cadence was based on simulations of ephemeris sampling under nominal CFHT observing conditions. The simulations determined the cadence required to reduce the nominal fractional semi-major axis uncertainty,  $\sigma_a$ , to the level required for secure dynamical orbital classification within two years of first detection. The orbital uncertainty reduces in a complex fashion, dependent on total arc length observed, number of observations, time of these observations relative to the opposition point, and an object’s heliocentric distance: closer objects benefit from a larger parallactic lever arm due to the Earth’s motion. The

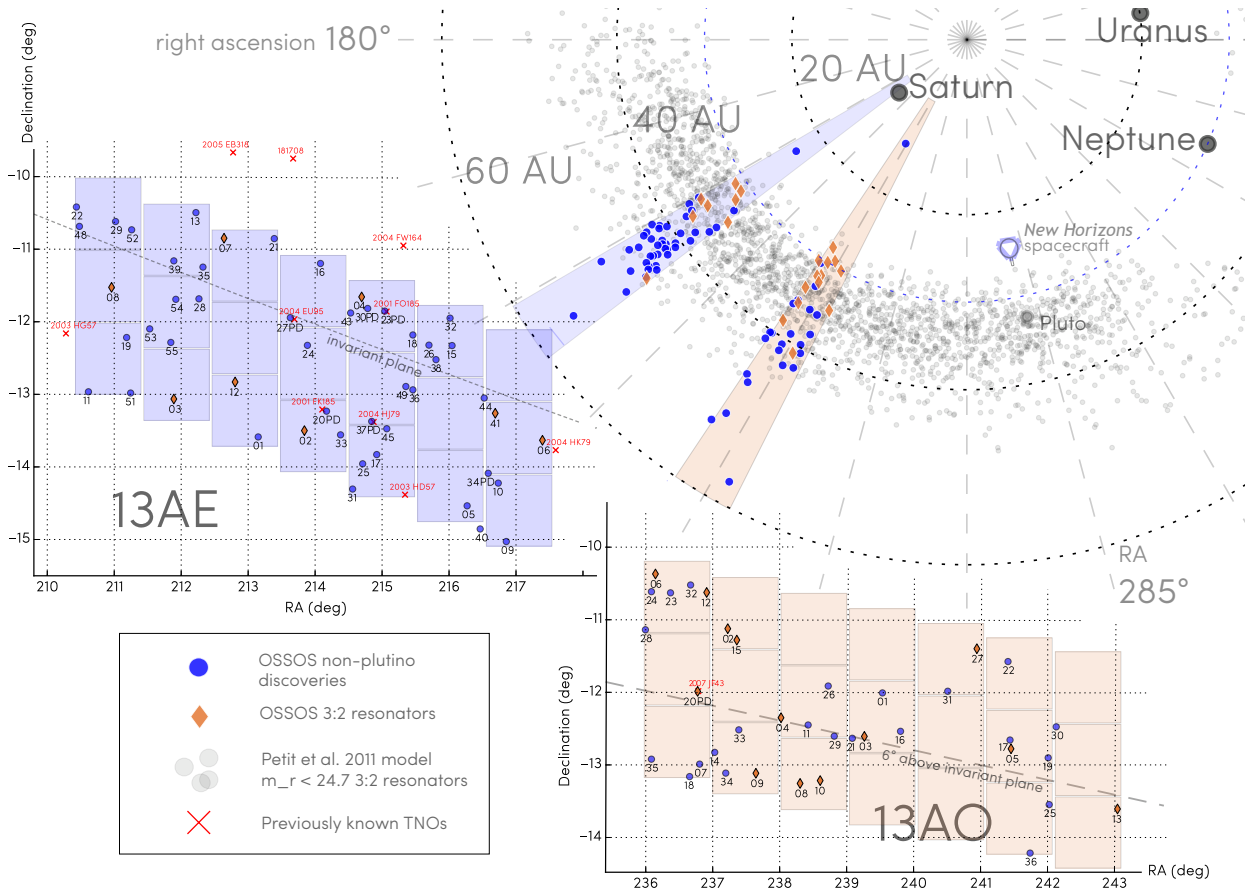


Fig. 1.— The first-quarter survey coverage for OSSOS relative both to the geometry of the Solar System (top right) and to the sky (top left and bottom right), at the time of the discovery observations in 2013 (blue: 13AE, orange: 13AO). Characterised discoveries (§ ??) are labelled with the last two digits of Table 3 for their respective blocks. The on-plane 13AE block contains more discoveries than the higher-latitude 13AO block (orange) due to the cold classical Kuiper belt’s concentration in the plane. The grey background points in the top right view show a prediction of the position density of plutinos (objects in the 3:2 resonance with Neptune) with instantaneous  $m_r < 24.7$ , as modelled by (Gladman et al. 2012). The visible model population is biased by detection proximate to perihelion. Plutinos avoid the longitude of Neptune due to the resonance’s protection mechanism. The discoveries show the survey’s sensitivity to plutinos (orange diamonds). 13AO is at higher inclination and closer to the angle from Neptune where objects in exact 3:2 resonance reach pericenter, and thus yielded a higher fraction of plutinos (orange diamonds) (13/36 TNOs), than in 13AE (8/49 TNOs).

cadence we selected ensured resonant identification was probable in the discovery year, with the second year’s observations needed to determine the libration amplitude with reasonable precision. A survey of 32 deg<sup>2</sup> in 2011-12 by Alexandersen et al. (2014) showed that this mode successfully provided classifiable orbits within two years of discovery.

Resonance dynamics require that resonant objects come to pericenter at a set longitude relative to Neptune (e.g. Volk et al. submitted, 2015). This confines the sky locations of their perihelia to a restricted range of ecliptic longitudes. Each OSSOS block location (listed in Table 1) was placed at ecliptic longitudes that maximize the detections of objects in certain low-order resonances with Neptune. The exact on-sky block placement is chosen to avoid chip-saturating stars brighter than  $m_r = 12$  and TNO-obscuring features like open clusters. We also avoid placement near the galactic plane, due to severe stellar crowding in this region. Extracting the complex biases that this sky placement causes on the detection of objects from the underlying population (Gladman et al. 2012; Lawler & Gladman 2013) is accounted for by the OSSOS survey simulator (§ 5.2).

A pair of blocks was observed in each half-year CFHT semester. Each semester’s pair was sited to maximize sampling of populations that occupy a range of inclinations. One block targeted the highest density of KBOs, which centres closer to the invariable plane (Souami & Souchay 2012) than to the ecliptic (Chiang & Choi 2008; Elliot et al. 2005; Brown & Pan 2004; Collander-Brown 2003), though more low-inclination objects are needed to be able to define the Kuiper plane warp as a function of increasing semi-major axis (Chiang & Choi 2008). The other block was placed between five and ten degrees off the invariable plane.

## 2.1. Observing parameters

The OSSOS discovery and tracking program use the CFHT MegaPrime/MegaCam (Boulade et al. 2003). In 2013 and 2014, the MegaPrime/MegaCam focal plane was populated by thirty-six  $4612 \times 2048$  pixel CCDs in a 4 by 9 arrangement, with a  $0.96^\circ \times 0.94^\circ$  unvignetted field of view (0.90 deg<sup>2</sup>) and 0.05” full-width-half-maximum (FWHM) image quality (IQ) variation between centre and edge. The plate scale is 0.184” per pixel, well sampling the 0.7” median seeing at Maunakea.

We observed our 2013 discovery fields in MegaCam’s  $r$ .MP9601 filter (564–685 nm at 50% transmission; 81.4% mean transmission), henceforth referred to as  $r$ , which is similar to the Sloan Digital Sky Survey  $r'$  filter (see § 3.5). Using this filter optimizes the tradeoff between reflected solar brightness (TNOs have colours  $B-R \sim 1-2$  (Hainaut et al. 2012)), the telescope’s and CCDs’ combined quantum efficiency curve, and sky brightness. The  $r$  band

Table 1. Target regions for the OSSOS survey

Block	RA (°)	Dec (°)	Ec. lat. (°)	Angle from Neptune (°)	Grid layout	Expected observation
AP	202.5	-7.8	1.5	-135	4 x 5	2015-04
AE	213.9	-12.5	1.0	-119	3 x 7	2013-04; this work
AM	233.8	-12.2	6.9	-105	4 x 5	2015-05
AO	239.5	-12.3	8.0	-94	3 x 7	2013-05; this work
BS	7.5	5.0	1.6	31	4 x 5	2015-09
BL	13.5	3.8	-1.8	41	3 x 7	2013-10
BH	22.5	13.0	3.3	51	3 x 7	2014-10
BD	48.8	16.5	-1.5	74	4 x 5	2015-11

Note. — Block names indicate half-year semester of discovery opposition (A for Northern spring, B for Northern autumn), followed by a distinguishing letter. Once discovery observations are successfully made, the block name is prefixed with the year of discovery opposition, e.g. 13AE. Coordinates are the center of each block at the time of anticipated targeting for discovery when the block reaches opposition. Angle from Neptune is approximated to projection to the ecliptic at the time of anticipated targeting for discovery: positive angles lead Neptune, negative angles trail Neptune.



delivers the best IQ distribution at CFHT and minimizes IQ distortion from atmospheric dispersion, especially useful as tracking observations often occur months from opposition when the airmass will be  $> 1.3$ . Obtaining all discovery observations using the same filter simplifies the design of the survey’s simulator (§ 5) and avoids object-color based biases in tracking.

Our integration length was set at 287 s. This exposure time reduces loss of signal-to-noise (SNR) due to trailing, aiding the detection of TNO binarity. This exposure length achieves a target survey depth of  $m_r = 24.5$  in median CFHT seeing. The number of fields in a block is set by the requirement of being able to observe one-half of a block three times (three observations provide the minimal initial orbital constraints for discovery) in three hours, the maximum time over which both airmass and IQ stability can frequently be maintained. Given the 40 s MegaCam readout overhead on top of the integration time, this requirement lets us set a grid of approximately 20 fields per block, with the exact number set to give a symmetric grid. The survey target depth allows detection of plutinos with radii larger than 20 km at their perihelion (per Luu & Jewitt (1988); assuming a 10% albedo per Mommert et al. (2012); Peixinho et al. (2015)), potentially examining the size distribution where models (Kenyon & Bromley 2008; Fraser 2009) and observations (Bernstein et al. 2004; Fraser & Kavelaars 2009; Fuentes et al. 2009; Shankman et al. 2013; Alexandersen et al. 2014; Fraser et al. 2014) suggest a transition in the size distribution.

MegaPrime/MegaCam operates exclusively as a dark-time queue-mode instrument for CFHT. The OSSOS project thus has between ten and fourteen potentially observable nights each month for observations, weather considerations aside. Through CFHT’s flexible queue-schedule system we requested our observations be made in possibly non-photometric conditions (discussed in § 3.5) with 0.6–0.8” seeing and  $< 0.1$  magnitudes extinction for discovery, and requested image quality of 0.8–1.0” seeing for followup observations. Images were taken entirely with sidereal guiding and above airmass 1.5. This aided the quality of the astrometric solution and the point spread function, and retained image depth: extinction on Maunakea is 0.010 mags per airmass.

## 2.2. Cadence

The OSSOS project has introduced a dense (for outer Solar System surveys) observing cadence to provide tracking observations that enable orbital solutions within the discovery year. In the discovery year we observed in each lunation that a given block is visible. These observations evenly bracket the date of the block’s opposition: precovery in the months before, discovery observations at opposition, recovery in the months after (Fig. 2). Precovery

and recovery observations on each field of each block were either a single image or a pair of images spaced by at least an hour. Each field of a block was imaged at least nineteen times in the discovery opposition.

The MegaCam mosaic has  $13''$  (70 pixels) gaps between each CCD and between the middle two CCD rows, and two larger gaps of  $79''$  (425 pixels) separating the first and last CCD rows from the middle two rows. To enable tracking of TNOs whose sky motions place them in the region overlapping these chip gaps, a dither was applied to some observations. We applied a north dither of  $90''$  to the observations at least once per dark run.

A typical sequence of observations in each lunation  $n$  leading up to the opposition lunation at time  $t$  was thus:

- $t - 3n$ : a single observation, another north-dithered single several days later
- $t - 2n$ : a single observation, another north-dithered single several days later
- $t - n$ : a pair of observations, either a single or another pair with north dither several days later
- $t$ : a triplet of observations, a single image a day later, and a north-dithered single image a day after that

The post-opposition sequence then unfolded in reverse. The original cadence simulation only tested  $t \pm 2$ , but adding  $t \pm 3$  became possible at times during observations (partly due to the ongoing nature of the survey operations, which could continue across CFHT semester boundaries).

During the discovery year the blocks were shifted over the sky at mean Kuiper belt orbital rates (Fig. 2). The shift rate was set at the mean motion of objects in the CFEPS L7 model (Petit et al. 2011); some  $3''$ /hour at opposition, declining to a near-zero shift away from opposition toward the stationary point. Almost all of the sample that is present within the block at discovery is retained through the entire year by this strategy. The shifting is done independent of any knowledge of the sky positions of the TNOs actually present in the field. This shift technique reduces the effects of orbit shear, reducing the ephemeris bias (Jones et al. 2010) in the tracked object sample.

The triplet of observations are the only data used for object discovery of a given block: they were acquired in the lunation that the block came to opposition. The triplet observations spanned at least two hours in the same night, with at least half an hour between each image of a field. Due to the length of observing time required, the triplet would generally

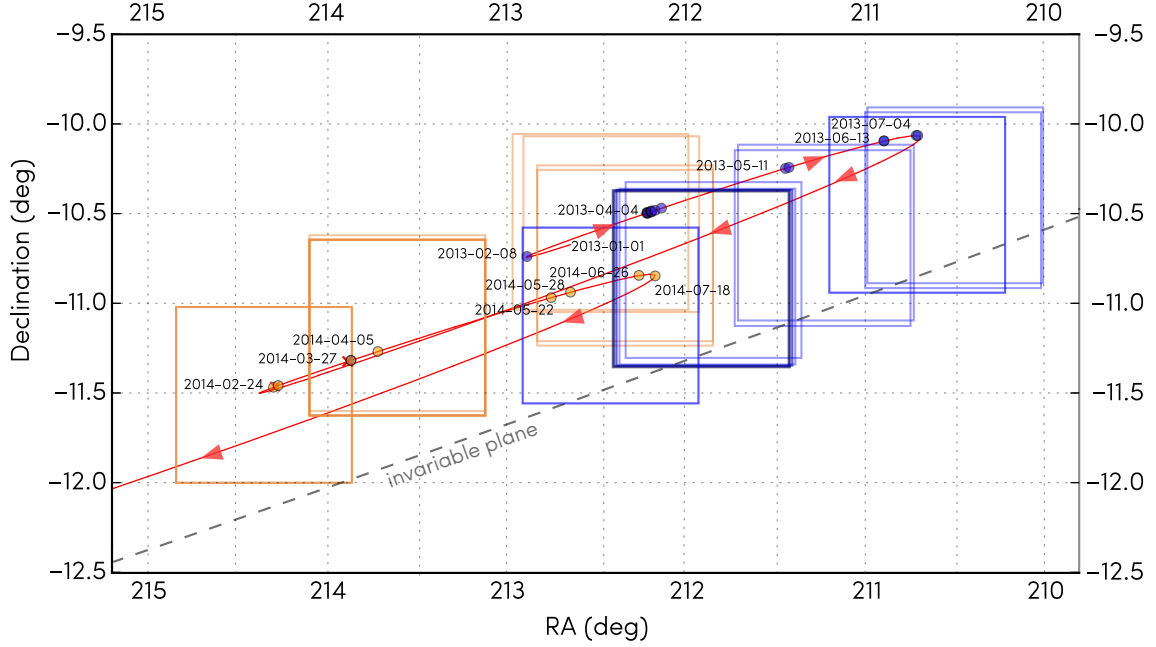


Fig. 2.— The cadence over 2013-2014 of OSSOS observations of a single 13AE field and the tracking of one of the TNOs discovered in that field, the insecurely (§ 6.4) resonant object  $\text{o3e13}$  (Table 3). Each box is an exposure of a 36-CCD MegaPrime square field of view. In 2013, the field centre was shifted at the Kuiper belt’s average sky motion rate (blue boxes). Note the dense observing cadence during the discovery opposition in April 2013 (heavier blue box due to overlap): the triplet of observations used for object discovery is on April 4, with other imaging April 5 and 6. In 2014, after the orbits for TNOs like  $\text{o3e13}$  were identified with multi-month arcs (§ 6.1), pointed recoveries (orange boxes) were made. Note that the pointed recoveries are not centered on  $\text{o3e13}$ , as the recovery pointings were chosen each lunation to encompass as many OSSOS TNOs as possible per observation. Dots indicate observations of  $\text{o3e13}$  (labelled by overall lunation for clarity; blue dots: 2013, orange dots: 2014), red line with red arrows shows the predicted position of  $\text{o3e13}$  from the survey start in Jan 2013 through into 2015.

be taken on half the fields of the block one night, and on the other contiguous half on a subsequent, often adjacent, night. The block location was shifted between these two nights, as part of our continuous shift strategy, reducing the chance that a TNO might be present in both half-blocks.

### 2.3. 2013A observations

This paper covers OSSOS blocks that had their discovery observations in 2013A. Forthcoming papers will cover the subsequent discovery observations (Table 1). The 2013A blocks were 13AE, centered at RA  $14^h20^m$ , DEC  $-12^\circ52'$  at discovery, spanning ecliptic latitude range  $b = 0 - 3^\circ$ , and 13AO, centered at RA  $15^h57^m$ , DEC  $-12^\circ30'$  at discovery, spanning ecliptic latitude range  $b = 6 - 9^\circ$  (Fig. 1). Being very close to  $90^\circ$  in longitude behind the ortho-Neptune point, 13AO is well placed to detect low libration amplitude 3:2 and 5:2 resonators where they are most likely to come to perihelion. The sky locations of the 13A blocks are at 44 and 30 degrees galactic latitude, comparatively close to the galactic plane for a TNO survey: the higher density of background stars increases the likelihood of occultations in the coming years as the OSSOS objects' astrometric positions descend into the galactic plane.

Consistent and uniform imaging conditions are a requirement of the OSSOS characterization process (§ 5). The OSSOS characterization provides a single detection efficiency dependent on magnitude and moving-object motion rate for each block of observations. Having uniform data quality within the block ensures that this characterization is sufficient for statistical analysis of object detection likelihoods. Proximity to the galactic plane increases the sky density of nebulosities and 13AO exhibited a uniformly elevated sky background from low-level nebulosity. Although Saturn was close to the top corner of the 13AE block (Fig. 1, blue block), the excellent rejection of off-field scattered light by MegaCam prevented much effect on the sky background of the overall mosaic, with the background of only the chip closest to Saturn affected. All the increased sky noise is characterized by our detection efficiency (§ 5). The 13AE discovery triplets were taken under some minor ( $< 0.04$  mag) extinction and with IQ that ranged from 0.65–0.84". The 13AO discovery triplets exhibited no extinction and IQ that ranged from 0.49–0.74".

The quality of detection is limited by the worst image in the triplet: frequently CFHT queue observing obtained two images at  $< 0.7''$  seeing and then the third would have degraded seeing. In cases where an image with  $> 0.8''$  occurred, the queue would re-acquire the discovery triplet. Such re-acquisitions turned the previous pair of quality-met images into tracking observations rather than being part of the discovery triplets.

Subsequent imaging to track the discoveries was acquired through August 2013. Not all discoveries were observed in every lunation due to falling in chip gaps or on background sources on some dates, faint magnitudes, or variable seeing in the recovery observations.

In much of 2013, poor weather conditions prevented observations in sufficient IQ for us to recover the faintest objects. To compensate, from November 2013 onward we used alternative 387 s exposures in  $0.8 \pm 0.1$  seeing for single-image passes on the block. This substantially improved the ease of later arc linkage on the discoveries (§ 6.1).

For the seven February-August lunations that the blocks were visible in 2014, the 13AE and 13AO discoveries were observed with pointed recoveries; this was possible because the high-frequency cadence in the discovery year shrank the ephemeris uncertainty to a tiny fraction of the MegaPrime field of view. A handful of fainter objects not immediately recovered in the first pointed recovery images were targeted with spaced triplets of observations in subsequent lunations until recovery was successful on all of them. Generally, two observations per object per lunation were made. The large camera field of view (FOV) allowed 2-10 TNOs to be observed per pointing through careful pointing choice. Each targeted pointing centre was shifted throughout the lunation at the mean motion of the discovered TNOs within the FOV, ensuring the targeted TNOs would be imaged. Combined with the non-linear improvement in object orbit quality (§ 6.3), which meant not all TNOs required imaging every lunation, we were able to make the necessary observations each lunation with fewer than the discovery opposition’s 21 pointings.

### 3. Astrometric and photometric calibration

Systematic errors and bias are the major limiting factor of current Solar System object astrometry. The astrometric measurements of TNOs reported here are tied to a single dense and high precision catalog of internally generated astrometric references. Use of a high-precision catalog will minimize or eliminate the astrometric catalogue scattering that Petit et al. (2011) encountered, allowing much more precise TNO orbital element determination.

In our OSSOS calibration, each sky block has a single coherent plate solution constructed; this is aided by the slowly retrograding field motion, which naturally produces extensive field overlap as the months progress, filling in all array gaps over the semester (Fig. 2). Objects with  $a = 30$  AU will move eastward  $\sim 2^\circ$  in a year, while sources at 60 au, where flux limits detection of all but the few largest objects, only move  $0.8^\circ$  per year, so the pointed recoveries in the second year of observation predominantly overlap and enlarge the existing grid from the first year. We create an astrometric grid with uniform photometric calibration across

the entire dataset for each block throughout our observing. We used **MegaPipe** (Gwyn 2008) with some enhancements. This grid uses stellar sources that are much brighter than almost all TNOs.

The astrometry was done in three steps, resulting in three calibration levels:

- Level 1: individual images were calibrated with an external reference catalogue. This was sufficient for initial operations in the data pipeline, such as object discovery, and object recovery at the end or during each dark run.
- Level 2: the source catalogues from the individual images were merged to produce a single internal astrometric catalogue, which was then used to re-calibrate each image. This step was repeated every few dark runs.
- Level 3: the images themselves were merged to produce a mosaic covering an entire block. An astrometric catalogue was generated from this combined image and used to re-calibrate each individual image. This step was run at the end of each observing season.

As each block’s images were brought to a higher level of calibration, the FITS headers of each image were replaced, allowing us to upgrade the TNO astrometry according to their  $(x, y)$  positions with the new world coordinate system (WCS), and the adjustment of the zero points of the photometry. The orbit classifications we provide in § 6.4, and the information we report to the Minor Planet Center, are from measurements relative to our final level 3 internal astrometric catalogue.

### 3.1. Level 1: individual image calibration

We detrended each image as it was taken each night of the dark runs, subtracting the bias and correcting the flat-field response. These preprocessed images contain a basic WCS and an ansatz zero point. An observed source catalogue was generated for each image with SExtractor (Bertin & Arnouts 1996), and cleaned of faint and extended sources. The cleaned source catalogue was then matched to the external astrometric reference catalogue. Once the observed source catalogue and the external astrometric reference catalogue were matched, the field distortion could be measured. This process is described in detail in Gwyn (2008). All OSSOS images have at minimum this level of calibration before any analysis is made. After Level 1 calibration, the astrometric residuals of the WCS are about 100 mas.

### 3.2. Level 2: merge by catalogue

The initial matching and fitting procedure was applied to the input images. The computed WCS was then applied to the observed source catalogues to convert the  $x, y$  pixel coordinates to RA and Dec. The RA/Dec catalogues were then combined to produce a merged astrometric catalogue covering the whole block. A given OSSOS field can be observed repeatedly on a single night (§ 2.2); including all the images would weight some parts of each field preferentially. Therefore, in such cases only the image with the best seeing was used to make the merged catalogue. For merging the catalogues, sources in two different catalogues were deemed to be the same object if their positions lie within  $1''$  of each other, irrespective of magnitude. To avoid confusion, no source is used if it has a neighbour within  $4''$ . Sources often lay in more than two catalogues, due to the drift of pointing centers from night to night (§ 2.2); all matches were grouped together. The result was a catalogue on the original reference frame (e.g. Sloan Digital Sky Survey (SDSS) (Ahn et al. 2014) or 2MASS (Skrutskie et al. 2006) corrected to UCAC4 (Zacharias et al. 2013)) but with smaller random position errors and a higher source density. This merged astrometric reference catalogue was then used to re-calibrate the astrometric solution of each individual image. This procedure was repeated two to three times, until the internal astrometric residuals stopped improving. The Level 2 calibration brought the astrometric residuals down to 60 mas.

### 3.3. Level 3: merge by pixel

To further enhance the internally generated astrometric reference frame, we generated a reference catalog from stacked images. In this step, the images with the updated Level 2 WCS in their headers were combined using SWarp<sup>1</sup>, producing a large stacked image covering an entire survey block. SExtractor was run on this stacked image to generate the final astrometric catalogue, and this catalogue was used to calibrate the original images. This image stacking step effectively combines all the available astrometric information from each star in each image at the pixel level. In contrast, the merge by catalogue method described in the previous section (and many other astrometric packages) only combines information about the centroids of the astrometric sources. The process is used to produce the final plate solution used in all OSSOS astrometry. The internal astrometric residuals were typically 40 mas after the Level 3 calibration, as shown in Fig. 3.

However, a few nearby or high-inclination TNOs (centaurs and some scattering objects)

---

<sup>1</sup><http://www.astromatic.net/software/swarp>

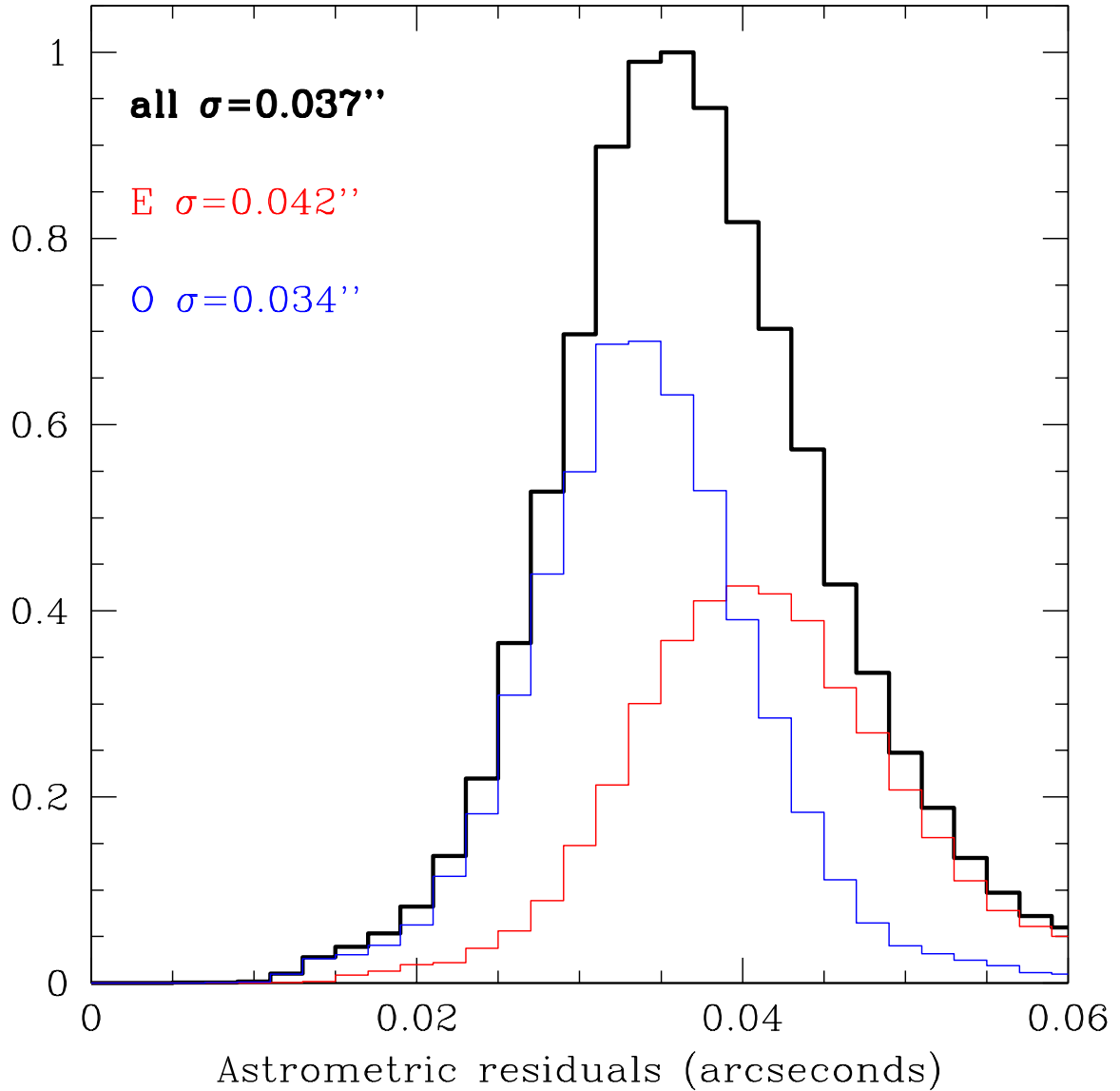


Fig. 3.— Astrometric residuals remaining in the background astrometric catalogue for OSSOS images after Level 3 (§ 3.3) plate solution calibration had been applied. These values are the residuals of the fixed sources in a catalogue from one image, relative to the sources in an overlapping image. The 13AO block is closer to the galactic plane than 13AE (§ 2.3): its higher density of sources causes the small  $0.008''$  improvement in residuals.



moved rapidly off the main block. These were re-observed in small, single-pointing patches off the main block. These pointings are stacked separately from the main block, resulting in a plate solution not tied directly to the solution for the main block. These measurements are thus less precisely connected to others. This only occurs, however, for objects that have large intrinsic motions and thus have easier-to-compute orbits, decreasing the impact of the less precise astrometry.

### 3.4. External astrometric reference catalogues

The internally generated catalogue provides a high-precision reference for our measurements; these highly precise measurements must then be accurately tied to an external reference system. The 13AE and 13AO blocks were not completely within the area imaged by the SDSS, which if available would have been used in preference due to its superior accuracy and depth. Instead, 2MASS was used, with corrections based on UCAC4. 2MASS is deeper than UCAC4 and therefore has a higher source density. However, there are small but significant zonal errors in 2MASS. When UCAC4 and 2MASS are compared, small zones of  $\sim 0.1''$  shifts between the two catalogues are apparent. The shifts occur with a periodicity of  $6^\circ$  in declination, corresponding to the observing pattern of 2MASS, which indicates that the errors lie in 2MASS (see Fig. 2 of Gwyn (2014)). Therefore we use the 2MASS catalogue which provides the source density needed to precisely link our internal catalogue to the external reference, corrected to the UCAC4 catalogue, which provide a more accurate translation to the International Celestial Reference System<sup>2</sup>.

#### 3.4.1. Proper motions

The mean proper motion of the stars is due to the motion of the Sun relative to the mean galaxy. Figure 4 shows the catalogued mean proper motion represented as vectors plotted in equatorial coordinates, computed by taking the median per square degree of the proper motions of all stars in the region in the UCAC4 catalogue. Neighbouring vectors from each square degree are close to identical. TNOs move only a few degrees over the course of the four-year survey, and thus differential proper motions do not measurably affect the internal astrometry.

Removal of individual stellar proper motions would improve the accuracy of the resulting

---

<sup>2</sup><http://www.iers.org/IERS/EN/Science/ICRS/ICRS.html>

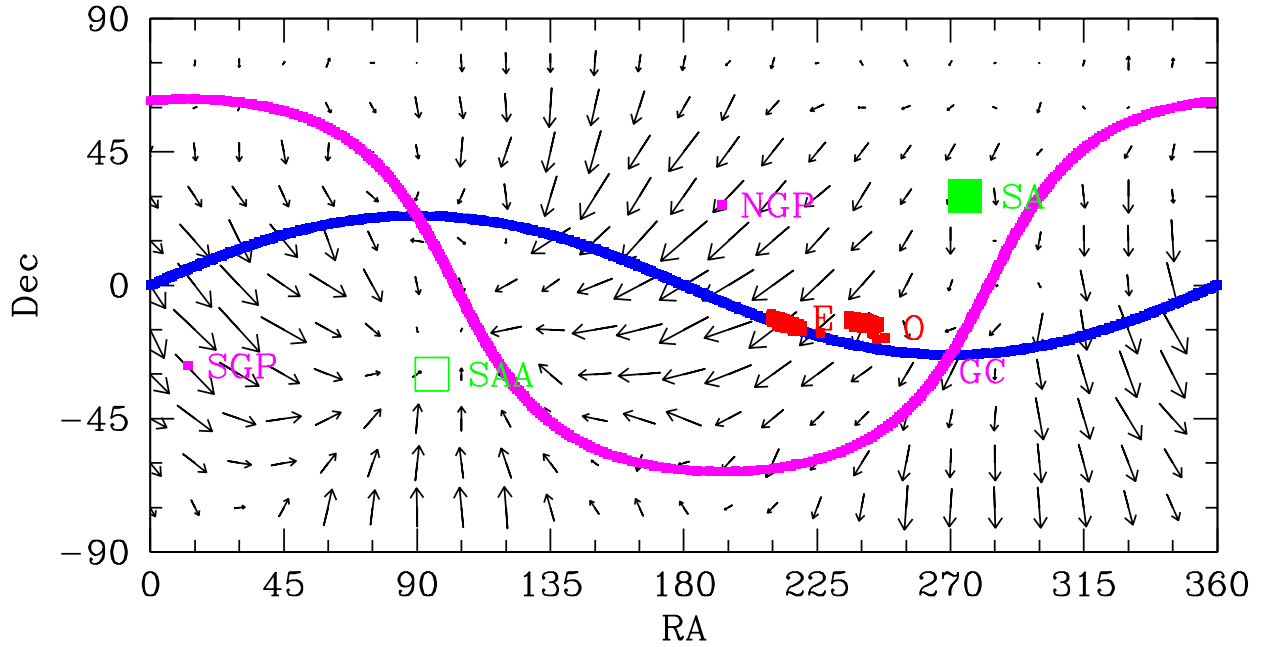


Fig. 4.— Mean proper motion of the stars in the background astrometric catalogue on the sky. The vectors indicate the mean proper motion of stars. The Sun is moving towards the solar apex (SA) (solid green square) and away from the antapex (SAA) (unfilled green square). In both panels, the ecliptic is shown in blue, the galactic equator in magenta, with the north galactic pole (NGP), south galactic pole (SGP) and galactic center (GC) indicated. The 13AE and 13AO blocks are red.

astrometric calibration. For the fainter sources that form the majority of the UCAC4, however, the individual proper motion measurements are too noisy. Figure 5 shows the proper motion of stars over a quarter of a square degree. The typical uncertainties on the proper motions are about 10 mas, which multiplied by the 10 year difference in epoch between UCAC4 and OSSOS, results in a 100 mas uncertainty in position. Furthermore, the individual proper motions are only known for the UCAC4 sources. The median annual proper motion on the other hand (in red in Fig. 5) is relatively well defined, and could be used to apply a systematic correction between the catalogues.

The corrections were therefore applied to each image by taking a subset of the UCAC4 and 2MASS catalogues from VizieR (Ochsenbein et al. 2000), determining the mean proper motion in that area, applying that to UCAC4, and matching the UCAC4 and 2MASS catalogues to each other. Working in  $0.2 \text{ deg}^2$  patches, the median shift between UCAC4 and 2MASS was then applied to 2MASS. A diagnostic plot, similar to Fig. 6, was produced for each image.  $0.2 \text{ deg}^2$  provided a good compromise: at smaller scales, the number of sources common to both catalogues drops to the point where the precision of the shift is less than the accuracy of the reference, leading to larger random error in the shift measurements; at larger scales, the zonal errors would average out, leading to larger systematic errors in the shift measurements. The corrected result was a catalogue as deep as 2MASS, but essentially as accurate as UCAC4.

As better astrometric catalogues become available, it may be possible to recalibrate the data. The first will probably be UCAC5, which should be available shortly (Zacharias, private communication), followed by Pan-STARRS and Gaia.

### 3.5. Photometry

The basis of the OSSOS photometric calibration is the SDSS. The SDSS photometry is converted into the MegaCam system using the following color term:

$$r_{Mega} = r_{SDSS} - 0.024(g_{SDSS} - r_{SDSS}). \quad (1)$$

For typical TNO colors  $g - r \sim 0.5\text{--}1.0$ , MegaCam  $r$  and Sloan  $r$  are thus separated by only 0.01–0.02 mags. The MegaCam zero-point varies from chip to chip across the mosaic. These variations are stable to better than 0.01 mags within a single dark run and are relatively stable between dark runs. The chip to chip variations are measured for each dark run by using any available images which overlap the SDSS footprint; because we are measuring the differential zero-point, it doesn't matter for this purpose if the night was photometric.

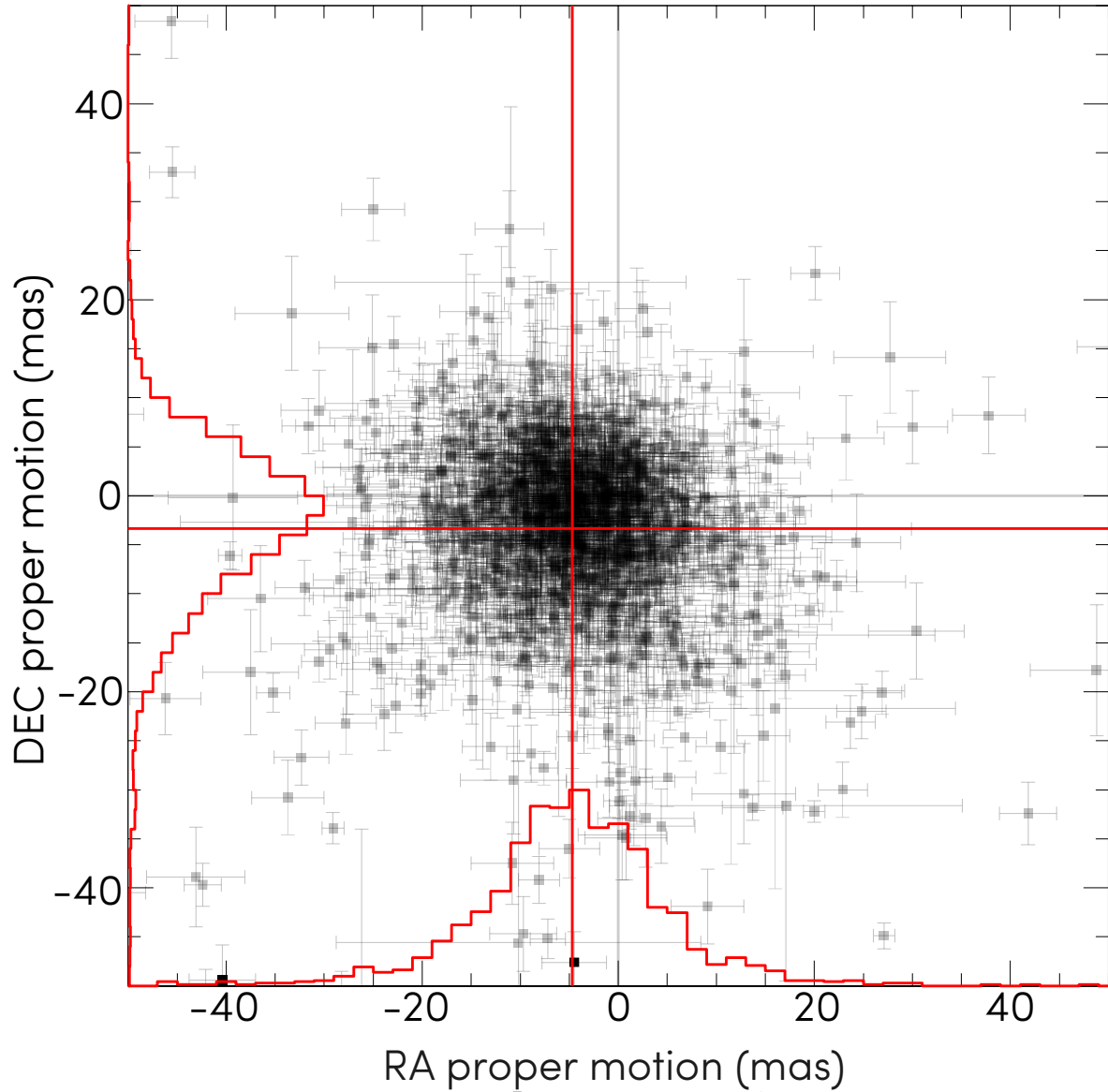


Fig. 5.— Example of individual proper motions of stars of the background astrometric catalogue over a quarter square degree. The black points show the individual proper motions and associated uncertainties for one year as measured by UCAC4. The red crosshairs indicate the mean proper motion for this patch of sky:  $-4.7$  mas in RA,  $-3.3$  mas in DEC. The red histograms shows the distribution of proper motion on both axes.

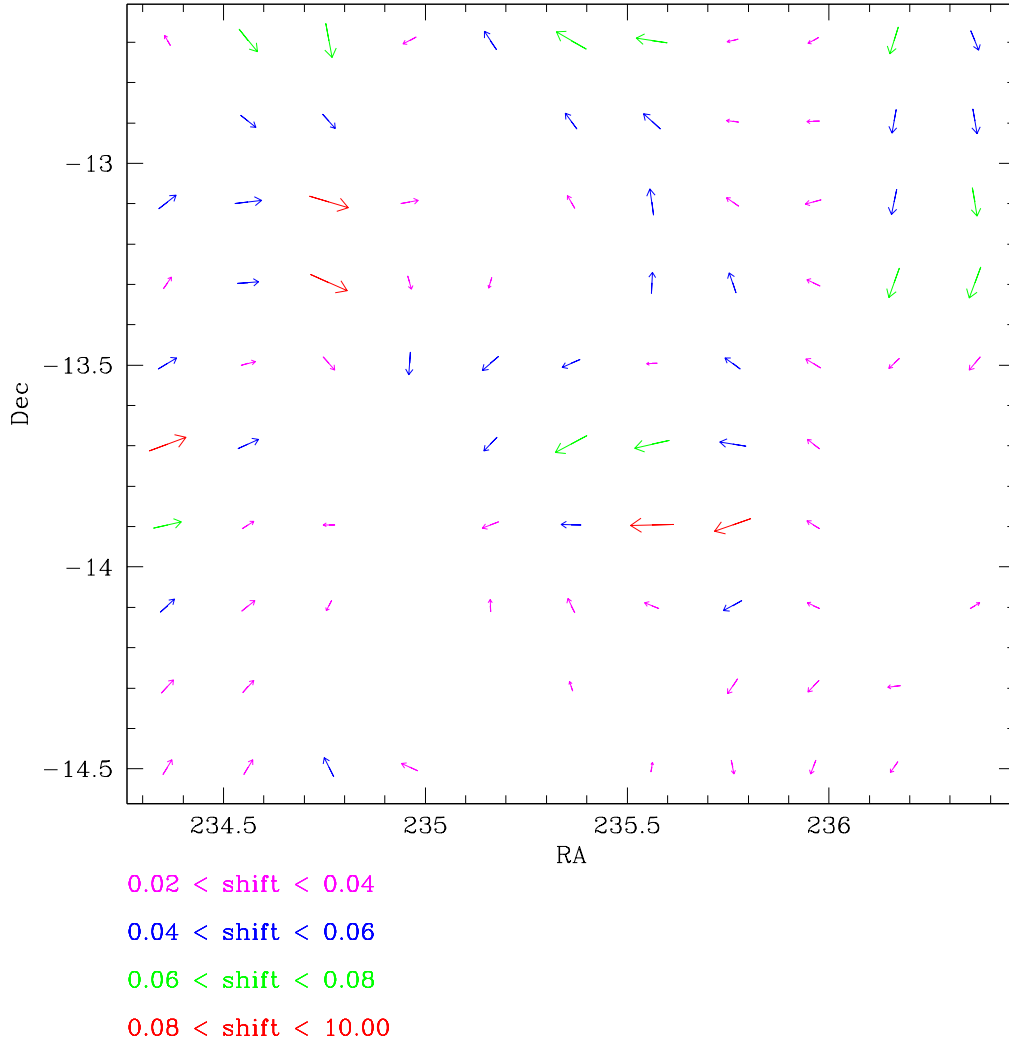


Fig. 6.— Example of correction of the stars in 2MASS by UCAC4. The vectors indicate the direction and relative size of the differences between 2MASS and UCAC4, measured in patches  $0.2^\circ$  on a side. The absence of a vector indicates that the shift was less than  $0.02''$ . The difference in size and direction of the shifts between adjacent  $0.2^\circ$  patches is small.

On photometric nights, all available images overlapping the SDSS were used to determine the overall zero-point of the camera for each night. OSSOS data taken on these nights which did not overlie the SDSS were calibrated using a combination of the mosaic zero-point computed nightly, and the differential chip-to-chip zero-point corrections computed for each dark run. The nominal MegaCam  $r$ -band extinction coefficient of 0.010 mags/airmass was used throughout.

The data acquired in non-photometric conditions were calibrated using overlapping images. The catalogues for each of the images were cross matched and the zero-point difference for each overlapping image pair was measured. The image overlaps are substantial; typically 2000 stars could be used to transfer the zero-point to a neighboring non-photometric image. The images overlapping with photometric images were in turn used to calibrate further images iteratively until an entire block was calibrated. At each iteration, the photometric consistency was checked. If a pair of ostensibly photometric images were found to have a large ( $> 0.02$  mag) zero-point difference, both were flagged as non-photometric and re-calibrated in the next iteration.

At Level 1 (§ 3.1), the photometric accuracy is 0.01 for images on the SDSS. For images not overlying the SDSS, the accuracy falls to 0.02–0.03 mags if the images were taken under photometric conditions. By Level 3 (§ 3.3), the internal photometric zero-point calibration between images within a block using this method is accurate to 0.002 mags RMS (Fig 7). The photometric residuals with respect to the SDSS are better than 1% (Fig. 7). Note that data are not directly calibrated with the SDSS, but rather that the ensemble of the SDSS is used as photometric standards.

#### 4. Data processing for discovery

The moving object discovery pipeline is designed to dig as much as possible down to the noise limit of the images, to find low-SNR moving targets while also generating minimal numbers of false positives. This strategy is critical because the steep TNO luminosity function means the majority of the detections occur at low to moderate SNR.

The OSSOS discovery pipeline follows nearly exactly on the methodology described in Petit et al. (2004) and used by the CFEPS project. This uses two separate processing streams, one based on source detection using SExtractor and the other based on identification of point-spread functions in wavelet space. Source lists for each image in a triplet are produced, matched and stationary sources are removed, then the remaining sources are searched for linearly moving objects. A few specifics of the original pipeline not described in Petit et al.

(2004) are detailed below. The complete OSSOS detection pipeline is open-source (§ 10).

Matching stationary-source lists requires some choices on the criterion of a match: we require sources to have matching spatial alignment, similar flux and similar size. These constraints are scaled relative to the FWHM of the first frame in the triplet. Additionally, when two sources in a single frame are found within one pixel of each other, they are merged. Visual examination of the merged source lists reveals that this matching algorithm does a reasonable job (90% of stationary sources are matched between frames) of matching galaxy and stellar centroids. The stationary sources are removed from further consideration.

TNO candidates are found in the images by trial linkages of non-stationary sources identified in the individual images. Each pipeline searched the list of non-stationary sources it had independently compiled by linking sources across triplets whose position changes were consistent with rates and angles of equatorial motion appropriate to the semester of observation. Apparent equatorial rates and angles of motion are dominated by the Earth’s orbital motion. For the 13A blocks, moving objects were retained within rate cuts 0.4–15 ”/hr, at angles of equatorial motion  $20^\circ \pm 30^\circ$  north of due west. For these blocks the parameters were set generously to ensure that they encompassed motions consistent with any detectable objects within 10-200 AU of the Earth.

The independent output of the SExtractor-based and the the wavelet-based branches of the pipeline each produced their own list of candidate moving objects. Both methods produce large numbers of false candidates; however, the false candidates are mostly different, such that taking the intersection eliminates most false candidates (Petit et al. 2004). The final moving object candidate list was formed by the intersection of the two lists. To be kept, the two lists must agree that the three sources in the candidate triplet all match in sky location to within one FWHM. This final list was then vetted by visual inspection.

## 5. Survey characterization

We use the definition that a trans-Neptunian object survey is *characterized* if it measures and makes available its pointing history and detailed detection efficiency as a function of apparent magnitude and rate of motion. This is potentially sufficient for luminosity function surveys (Petit et al. 2008). However, to be a characterized orbital survey, a survey also needs to minimize ephemeris bias; otherwise systematic biases can be introduced into the derived orbital distribution (Kavelaars et al. 2008; Jones et al. 2010). We detail all the needed information for OSSOS. This provides the characterization needed by our survey simulator, which allows quantitative comparison between proposed cosmogonic models and

the detections of the survey.

### 5.1. Detection efficiency

The detection efficiency of distant moving objects is a function of their apparent magnitude and their rate and direction of motion on the night of the discovery triplet observations. We characterize this detection efficiency by implanting tens of thousands of artificial PSF-matched moving objects in a temporally scrambled copy of the data set, and running object detection in a double-blind manner. Additionally, we use a novel method to obtain an absolute measure of the false positive rate.

First, we create a copy of the detection triple and then re-arrange the time of acquisition in the three discovery image headers, shuffling the three images to the order 1, 3, 2. These images are passed through the software detection pipeline. Any source that is found in a time-scrambled set that was not implanted must be false; no real outer Solar System object reverses apparent sky motion in two hours. Any such detections thus provide an absolute calibration of the false-positive rate (Alexandersen et al. 2014). Secondly, we then plant a huge number of artificial objects into this time-scrambled copy and pass that through the pipeline. In the implanted copy, any detections must thus either be either artificially injected or false positives; none can be real. Characterizing the detection efficiency in the scrambled data also avoids planted sources obscuring detection of real ones. In the 13A data, 43,000 sources were implanted per block (57 per CCD).

Each CCD thus has three sets of moving candidates, each from running a distinct set of three images through the detection pipeline:

- from the **discovery** images: potential discoveries;
- from the temporally **scrambled** discovery images (which have no planted sources): if accepted through the next stages of evaluation these become *false positives*;
- from the temporally scrambled and **planted** images: planted discoveries, which if subsequently rejected are *false negatives*.

We discuss the classification of false positives and false negatives in context below. The detection pipeline produces 2268 sets of moving candidates per block (3 sets for each of 36 CCDs in each of the 21 fields of 13A’s block grid), which are stored in a central repository.

The moving candidates are assessed by visual inspection, in two phases. Our interface is configured as a model-view-controller stack, using `ds9` as the windowing GUI. The images



are stored on a cloud server and image stamps retrieved as needed (Kavelaars 2013). The interface maximizes agnostic presentation of these candidates at all times: each person is sequentially presented with the candidates from a randomly selected set, so that they do not know the nature of the set being inspected. During evaluation, the set is locked to that person, and released back to the pool if the person exits the interface before evaluating all sources in the set. If fully evaluated, the set’s metadata are updated and the results of the inspection uploaded to the central repository. This robustly supports multiple people simultaneously examining a block’s discovery characterization. There is remarkably little variation in detection efficiency between people (Fig. 8); most importantly, there is strong agreement on the characterization threshold (specified below).

Spurious candidates are thoroughly suppressed by the detection pipeline (Petit et al. 2004). The most common type of spurious candidate that survived through to rejection in the first phase of visual inspection was due to a candidate being formed from background noise popping above the noise threshold in three places, approximately linearly spaced with time. These false detections are easily recognized and rejected by visual inspection. The second frequent spurious-candidate class were bright spots along diffraction effects that happened to align, within the allowed angles of movement (§ 4) across the image. These are also easily identified during the first round of inspection.

The second visual inspection evaluated the remaining moving object candidates. For resilience, this second examination was preferentially done by a different person. False positives are any candidates from a scrambled set that survived the second examination. False negatives are any planted candidates that were successfully identified by the automated pipeline, but then (incorrectly) rejected during either of the visual inspections. The false negative rate produced during the twofold visual inspection was zero brightward of the characterisation limit (discussed below): the pipeline detection efficiency is not weakened by the addition of visual inspection.

The second visual examination measured aperture photometry with `daophot` (Stetson 1987) of all accepted candidates. We manually assigned standard flags from the Minor Planet Center<sup>3</sup> to the photometry and astrometry of the candidates from the discovery images. These are needed both for the survey simulator and for wider use of the objects’ photometry, e.g. light curves. These measurements defined the discovery triplet for each object.

At the bright end,  $m_r \sim 21$ , the fraction of planted sources recovered by the entire process does not reach 100%, as about 10% of the sky is covered by stars at OSSOS magnitudes.

---

<sup>3</sup><http://www.minorplanetcenter.net/iau/info/ObsNote.html>

If a moving object transits any fixed source in one of the three images, it tends not to be found by the automated search algorithms unless much brighter than the confusing source. A gradual drop in efficiency occurs with increasing magnitude due to the increased frequency of stellar/galactic crowding.

At a certain magnitude depth in the images, about  $m_r \sim 24$  for OSSOS, the SNR and thus the efficiency with which we can detect sources rapidly falls off, setting a natural completeness limit in magnitude. Petit et al. (2004) determined that fainter than  $\sim 40\%$  efficiency, a person is no longer confident that the pipeline’s moving candidates are real; a small error in the characterization at these low efficiencies would result in a large effect in the subsequent modelling. After all the candidate sets for a given block were examined (Fig 8), a function was fitted to the aggregate of the raw efficiencies produced from each person blinking the planted sets of the 756 chips per survey block (Fig. 9). The crucial efficiency versus magnitude behavior is fit to the formulation (shown graphically in Fig 9)

$$\eta(m_r) = \frac{\eta_o - c(m_r - 21)^2}{1 + \exp\left(\frac{m_r - m_L}{w}\right)}$$

where  $\eta_o$  is roughly<sup>4</sup> the efficiency at  $m_r = 21$ ,  $c \sim 0.5\%$  measures the strength of a quadratic drop, which changes to an exponential falloff over a width  $w$  near the magnitude limit  $m_L$ , similar to that used by Gladman et al. (2009, eq. 2). This function better fits the OSSOS detection efficiency than does the frequently used hyperbolic tangent function (Gladman et al. 1998; Trujillo et al. 2001).

The parameters we obtained for the motion-rate range  $0.5\text{--}7''/\text{hr}$  for 13AE were  $\eta_o = 0.89$ ,  $c = 0.027$ ,  $m_L = 24.17$ ,  $w = 0.15$ , and for 13AO were  $\eta_o = 0.85$ ,  $c = 0.020$ ,  $m_L = 24.62$ ,  $w = 0.11$ .

We used this fit to set our *characterization limit*: the magnitude above which we have both high confidence in our evaluation of the detection efficiency, and find and track all brighter objects. This is not at a fixed-percentage detection efficiency, unlike in Jones et al. (2006), Kavelaars et al. (2009) or Petit et al. (2011), but rather set more stringently at the apparent magnitude where OSSOS ceased reaching 100% tracking efficiency due to low flux. In practice this was usually close (Fig. 9) to the magnitude where the detection efficiency falls to 40%. The characterization limit is dependent on the moving object rate of motion: our limits are listed in Table 2.

No false positives, nor any false negatives, that were brighter than the characterization limit survived the two-stage visual assessment process. This asserts that our efficiency

---

<sup>4</sup> $\eta_o$  is the efficiency at  $m_r = 21$  in the case where  $\exp((m_r - m_L)/w) \lll 1$ .

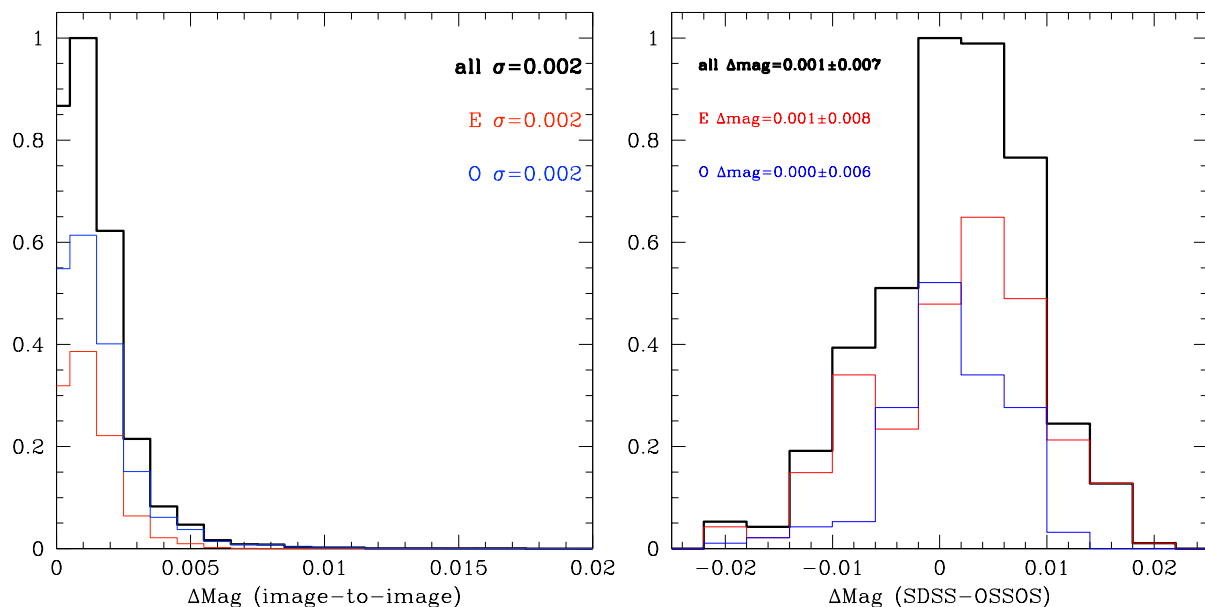


Fig. 7.— Photometric residuals of the background astrometric catalogue of the 13AE and 13AO blocks. Left: internal image-to-image residuals; right: overall residuals with respect to the SDSS.

Table 2. Characterization limits for the 13A blocks of the OSSOS survey

Motion rate (″/hr)	Characterization limit ( $m_r$ )	Efficiency at limit (%)
13AE		
0.5–8.0	24.09	37
8.0–11.0	23.98	40
11.0–15.0	23.86	41
13AO		
0.5–7.0	24.40	55
7.0–10.0	24.43	41
10.0–15.0	24.27	41

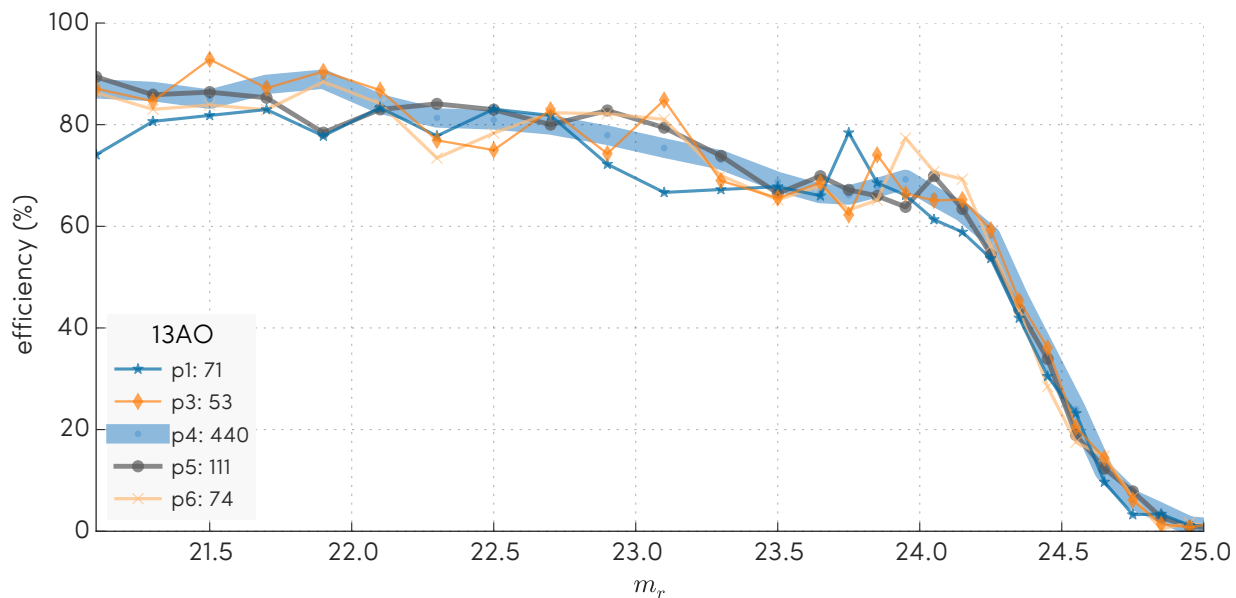


Fig. 8.— Raw unsmoothed individual participant detection efficiencies for 13AO: the fraction of artificial objects implanted in a time-scrambled copy of the discovery triplet images that are recovered by each person  $p_i$ , as a function of  $m_r$ . The number of CCDs reviewed by each person sets the line weight for their data and is indicated in the legend. This shows the effect on the overall detection efficiency output from each person’s contribution. There is agreement in detection efficiency between people, especially at the fainter magnitudes critical for characterisation, where more artificial objects were planted due to the steepening TNO luminosity function.

function is of high accuracy and unpolluted.

Fig. 9 illustrates the variation in sensitivity to different angular rates of sky motion. Our survey is optimized for detection of objects at Kuiper belt distances: this is reflected in the greatest detection efficiency for objects when they are moving with rates of 0.2–8 "/hr. This gives us sensitivity out to distances out to  $\sim 300$  AU, at which on a circular orbit, an object would move  $\sim 0.5$  "/hr. For close, fast-moving objects ( $> 10$  "/hr), sensitivity is maintained until magnitudes that are a little brighter than the efficiency at Kuiper belt distances (Fig. 9). As an additional proof of our sensitivity to centaurs, the proximity of Saturn to the 13AE block placed a few known satellites on one field of 13AE. Our analysis recovered the irregular satellite Ijiraq at 9.8 AU (Fig. 1), the only moon above the 13AE magnitude limit, exhibiting some minor and expected elongation along its direction of motion.

All objects listed in the MPC that fell on the survey coverage of the discovery triplets were recovered, as seen by the overlapping of symbols in Fig. 1 and noted in Table 3. While 2003 HD57 may look undetected in Fig. 1, it was in fact two pixels south of the first image of the 13AE discovery triplet. These recoveries of known objects aid our confidence in our measured detection efficiency.

## 5.2. Survey simulator

The OSSOS survey simulator is the key to allowing the collected sample of trans-Neptunian objects to be debiased and used to constrain the true underlying population. It subjects a theoretical model of the orbital and size distribution to the same calibrated detection and tracking biases that were imposed on the real TNOs during the observational survey, after which the probability of that model can be assessed.

The simulator has three input components: the telescope pointings and dates used for the observations, the detection efficiency from the analysis of the discovery observations, and the objects discovered by OSSOS.

We use the pointings recorded for the discovery triplets to determine the area of sky that was searched by the survey. MegaPrime’s focal plane (Sec. 2.1) sets the size of each field in the survey simulator. The filling factor of an image is 0.9164 due to the gaps between active parts of the CCDs. This filling factor is then multiplied by the fractional coverage determined for each block due to any pipeline processing failures; this fractional coverage was 99.07% on 13AE and 98.81% on 13AO. Processing failures of these chips include poor builds of PSFs and failure to align between images of the triplet.

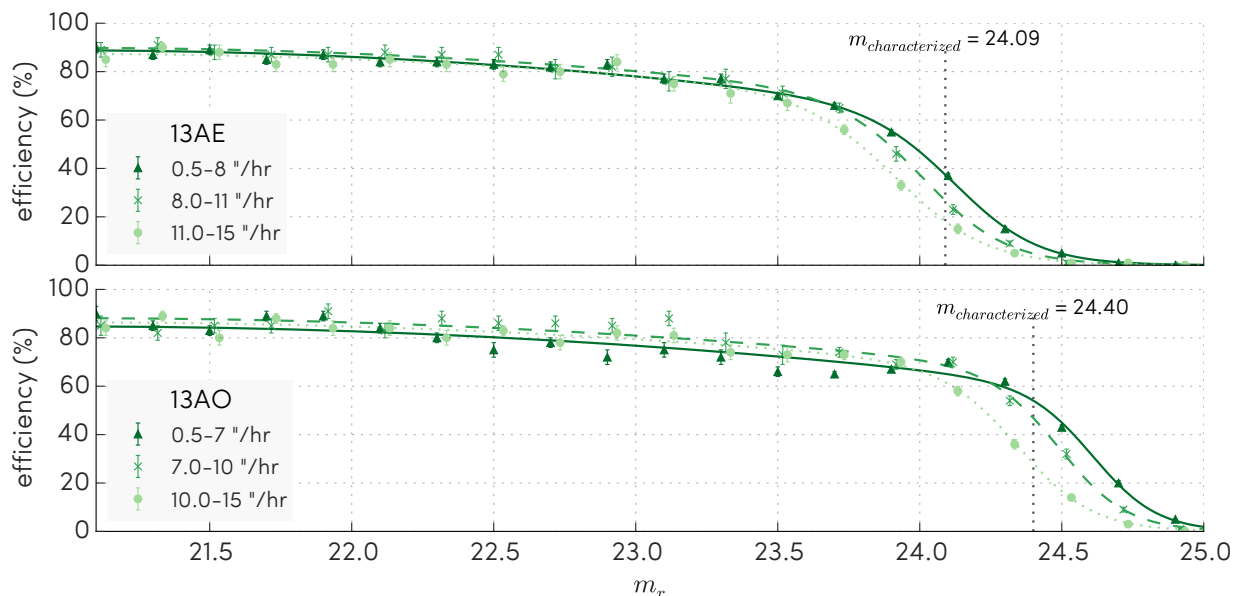


Fig. 9.— Total combined OSSOS detection efficiency in each 13A block: fraction of planted sources recovered by the overall data reduction as a function of magnitude and rate of apparent sky motion. The efficiency begins below 100% due to loss of sources to merges with background sky sources and to chip gaps. Background confusion gradually increases for fainter magnitudes. Faster-moving objects are more affected by movement off the field during the temporal span of the discovery triplet. 13AO had better IQ during the observation of the discovery triplet, pushing its limiting magnitude deeper.

*Characterized* discoveries, those brighter than their block’s characterization limit, form the set of comparison objects in the survey simulator. The luminosity functions of the various dynamical classes have been shown to be well represented by steep power laws within the magnitude range we study, with the number of objects per square degree on the ecliptic that are brighter than a magnitude  $m$  given by  $\Sigma(m) = 10^{\alpha(m-m_o)}$  with  $\alpha = 1.5_{-0.2}^{+0.4}$  for the cold population and  $\alpha = 0.87_{-0.2}^{+0.07}$  for the dynamically hot population, and the normalization constant  $m_o \sim 23.4$  in  $r$  (Fraser et al. 2014). Moreover, there appears to be a divot or sharp change in the luminosity function slope at about the limit of our survey (see discussion in § 2.1). Hence it is important to precisely model the effects of the magnitude on object detection. To proceed, we must make the distinction between the intrinsic magnitude of an object and its measured magnitude. The intrinsic magnitude corresponds to the average flux of the source that reach the detector, while the measured magnitude corresponds to what is measured on a single frame accounting for Poisson noise in the source and in the background. For determining the efficiency function, we implant fake objects in the images according to a chosen intrinsic magnitude, which is how the efficiency is defined. When we simulate the detection of a model object, we work in intrinsic magnitude space. When an object is declared detected, we then compute a measured magnitude (see § 11), decide if it would be above the characterization limit, and finally compare the measured magnitudes of the planted model and real detected objects. This does however not account for object rotational variability, though taking our discovery observations over a two-hour baseline should help somewhat. A follow-up program to comprehensively measure rotational variability would help to refine our final results.

## 6. Orbits

The loss of discovered objects by failing to track them, either because they had weakly predicted locations or because tracking wasn’t done until precise classifiable orbits were achieved, results in a biased view of the orbital distribution (ephemeris bias). The OSSOS goal is to eliminate this bias by tracking virtually all outer Solar System detections with magnitudes above each block’s characterization limit. This was achieved for all objects above the 13A characterization limits.

### 6.1. Arc extension

Objects found by OSSOS must have their many observations converted into an orbit. Following discovery in the opposition triplet, we knit together observations of each object

from every lunation into longer orbital arcs, starting within the discovery lunation and working further out in time. This iterative procedure started at each stage with an orbital fit to the accumulated observations, using the Bernstein & Khushalani (2000) algorithm. This orbit and its uncertainties were then used to query the archival image search tool Solar System Object Image Search (Gwyn et al. 2012)<sup>5</sup> for further available OSSOS imaging containing the object. This tool identifies all available archived imaging, but as OSSOS is deeper than most previous wide-field imaging work, we have not yet made use of other datasets. Starting the initial search by only querying data near in time to the discovery kept on-sky uncertainties (and hence the number of images to examine) from greatly multiplying (Fig. 1, Jones et al. 2010). We then visually identified the TNO within or near the predicted  $1\text{-}\sigma$  on-sky error ellipse by comparison with OSSOS images of the same piece of sky at a different time, when the object would not be present. This additional astrometry was used to generate a longer-arc orbit, which was then used to request more OSSOS imaging in dark runs further from the detection triplet. We iterated until an arc over the entire discovery year was assembled. In the second year of observations, the first-year orbits usually provided such accurate ephemeris predictions (sub-arcminute  $1\text{-}\sigma$  on-sky error ellipses) that recovery was immediate rather than needing this iterative process. Those few objects which sheared off the block still had arcs for at least several lunations; in these cases the uncertainty at the start of the observations the following opposition were  $\sim 30$  arcmin, and a manual visual search resulted in the recovery of the object, which was then tracked through the entire second year.

## 6.2. Recovery success

Even though the locations of the objects were unknown when the first-semester observation suite was acquired, the slow drifting of the blocks at Kuiper belt mean-motion rates (§ 2) retained almost all objects within the observations. Independent of its characterization limit, each block has a *tracking fraction*: what fraction of the objects above the characterization limit were recovered outside of their discovery triplet and generated a high-quality orbit. We recovered 100% of our discoveries that were above the characterization limit in both 13A blocks. This is an improvement on previous characterized surveys, including CFEPS (Kavelaars et al. 2009) which did not image their discoveries every dark run through the discovery semester. The survey of Alexandersen et al. (2014) lost only two of 80 detections, one near a field edge, and one near the survey’s 40% efficiency cutoff. The 100% recovery achieved in the first quarter of the OSSOS survey means that ephemeris bias is absent and the sur-

---

<sup>5</sup>[www1.cadc-ccda.hia-ihp.nrc-cnrc.gc.ca/en/ssois/](http://www1.cadc-ccda.hia-ihp.nrc-cnrc.gc.ca/en/ssois/)



vey simulator (§ 5.2) can use the precise characterization information about the survey to quantify the flux, pointing, and detection biases (Kavelaars et al. 2008; Jones et al. 2010).

### 6.3. Orbit quality

Generally, for outer Solar System objects, the precision of orbits based only on the discovery opposition astrometry are too poor to allow follow-up using narrow-FOV cameras in the 2nd opposition. In contrast, extending each OSSOS object’s arc with all the images taken in the 13A discovery semester, resulting in an arc of 150–183 days, yielded preliminary orbits with fractional semi-major axis uncertainty of  $\sigma_a \sim 0.1 - 1\%$  (Fig 10). The small uncertainty was due to total arc, frequent sampling, and orbit-fit residuals of  $< 0.03''$ . This was sufficient to predict the object’s position on the sky in the next year to an ephemeris accuracy of a half-arcminute or better, predominantly  $< 10''$ . This is an order of magnitude better than that obtained by Petit et al. (2011). The ephemeris accuracy would be sufficient to target discoveries with larger-aperture telescopes, for measurements unrelated to orbit refinement, in the opposition immediately following discovery. Initial recovery in 2014 extended the arc to  $\sim 360$  days, dropping the fractional uncertainty for  $\sigma_a$  by a factor of 2-3 (depending on which lunations the objects were seen in 2013) to  $\sigma_a = 0.03\% - 0.3\%$  (Fig. 10). Later extension of the arc through 2014 brought the 13AE objects to a median  $\sigma_a = 0.03\%$  and a median  $\sigma_a = 0.07\%$  for 13AO; the difference is due to the existence of more observations per dark run for the 13AE block.

Some objects in particular converged quickly to  $\sigma_a < 0.1\%$ ; by early in 2014A, nearly half the objects in 13AE, particularly cold classicals, reached sufficiently high orbit quality that only sparse sampling throughout the remainder of the semester was required (Fig 10). The total number of observations on the objects varied between 14 and 55, though the median was 26; the number of observations is somewhat correlated with orbital quality (Fig 10), but the distribution of those observations in time is also important for the convergence of  $\sigma_a$ .

We note that the figure-of-merit  $\sigma_a$  is only a useful approximation that does not capture all aspects of orbit quality. For example, resonant libration amplitudes (discussed for OSSOS in Volk et al. submitted, 2015) have uncertainties that while dominated by  $\sigma_a$ , also depend on  $e$  and the accuracy of angles like the ascending node  $\Omega$  and the pericenter’s longitude  $\varpi$ . Location within the resonance also matters: an object with orbital elements on the edge of the resonance might need a much smaller  $\sigma_a$  to determine the libration amplitude to  $10^\circ$  precision than if its elements were near the center of the resonance.

Our milli-arcsecond astrometry on moving targets travelling several degrees across the

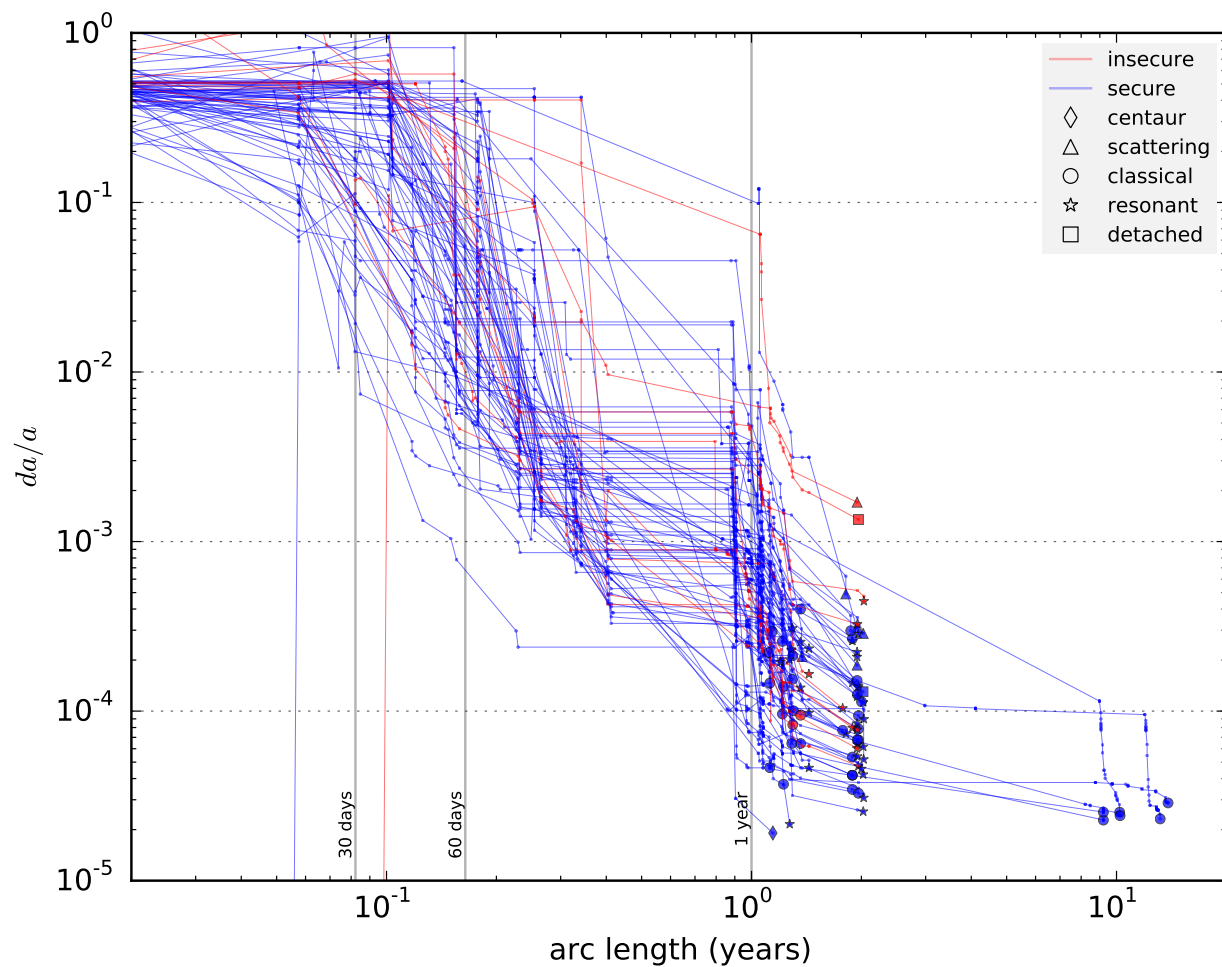


Fig. 10.— Fractional semi-major axis uncertainty  $\sigma_a$  of OSSOS objects as a function of arc length, as approximated using the Bernstein & Khushalani (2000) algorithm, for each astrometric measurement made by OSSOS. Final orbit classifications (end symbol on each object’s line) and corresponding security of that classification (line color) are those from the technique in § 6.4, given in Table 3. Previously discovered objects with decade-long arcs cluster at lower right.

sky is unprecedented. A major factor in the high quality of the OSSOS orbits is the use of a single astrometric solution over the entire area that a given block traces out over the two years of the survey. The high quality of these OSSOS astrometric catalogues eliminates nearly all of the astrometric catalogue scattering that Petit et al. (2011) encountered: the median OSSOS astrometric residuals around the best orbit fit are twofold lower than Petit et al. (2011)’s typical orbit-fit residuals of  $0.25''$  (Fig. 11). The catalogue approaches what the future Gaia catalogue will provide in absolute astrometry. Only for our very brightest objects is the astrometric scatter in the solution slightly worse than the centroid uncertainty — at the characterization limit, the residuals are centroid-limited. Further improving the internal astrometric solution’s scatter will therefore not result in improvement to the OSSOS orbit precision.

#### 6.4. Orbit classification

The classification scheme for the OSSOS detections is that described by Gladman et al. (2008), which we briefly summarize here. A best-fit orbit for each OSSOS detection is computed using the Bernstein & Khushalani (2000) algorithm. Maximum and minimum semi-major axis orbits consistent with the observations are found by searching the parameter space, starting at the best fit, via a Monte-Carlo method to identify an orbit in the 6-D parameter space with the two extremal values in  $a$ , which have residuals no worse than 1.5 times the best-fit orbit’s residuals.

These three barycentric orbits are converted to heliocentric, ecliptic coordinates and integrated forward in time for  $10^7$  years using the `rmvs3` subroutine within the SWIFT integrator package (Levison & Duncan 1994); the planets’ positions are taken from the JPL Horizon’s service (Giorgini et al. 1996) for the epoch of the orbit fit. These integrations are first checked for resonant behavior, defined as libration of a resonance angle of any resonance up to  $30^{th}$  order within 2% of the object’s average semi-major axis (see further discussion in Volk et al. (submitted, 2015)). Objects not resonant with any planet with  $a < 30$  AU are classified as centaurs. An object is classified as scattering if its semi-major axis varies by more than 1.5 AU during the integration. Objects with constant semi-major axis over the  $10^7$  year period are classified as detached if they have  $e > 0.24$  or as classical if they have  $e < 0.24$ . Classifications are considered *secure* if all three integrations for an object receive the same classification.

Orbital insecurity is a property of the known orbital parameters of characterised, fully tracked OSSOS discoveries. It is not necessarily due to poor-precision measurements; even with excellent ground-based data in  $0.5''$  seeing, there is a fundamental degeneracy to a suite

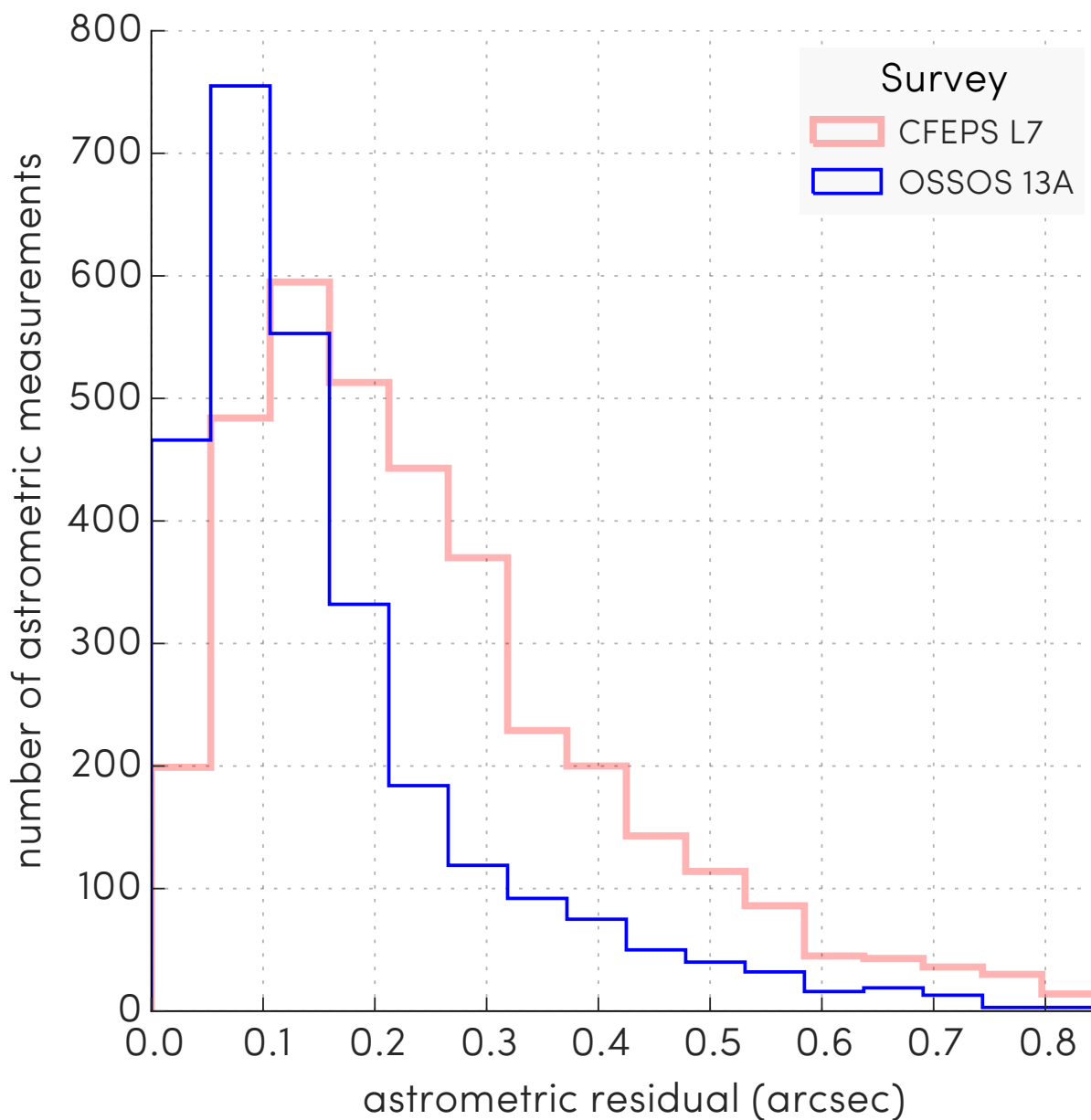


Fig. 11.— The astrometric scatter of OSSOS observations (median 124 mas; 2872 measurements) relative to the Bernstein & Khushalani (2000) algorithm best-fit orbits for the 13A discoveries. For reference, the distribution from Petit et al. (2011)’s detections (median 216 mas; 3643 measurements) is shown. Note that most of the detections have SNR < 10, and so the measurement accuracy is essentially the centroiding scatter on the faint targets: the OSSOS plate solutions are so accurate that catalog scatter has become irrelevant.

of orbits, all of which produce the same short-arc behavior. Most OSSOS objects were not secure in their first year of observation, when orbital arcs were usually 4 or 5 months long. The addition of even a single dark run in the second year usually resulted in a classical-belt object identification being secure. Secure resonant identification usually required the full suite of dark runs in both observation years. During the four-year duration of OSSOS, insecure objects will continue to be tracked until their classifications become secure; for example, ten of the 13A discoveries received another measurement in January and in March 2015 to improve orbital quality. All of the currently insecure classifications are due to proximity to resonances of at least second order.

The fraction of securely classified objects that we achieve within two years is 94%. In contrast, objects in the Minor Planet Center ensemble that have been observed since discovery with sparser cadences lack classifiability within this timeframe (Gladman et al. 2008).

## 7. Discoveries

Fig 12 shows that the general pattern of the orbital elements of the 85 first-quarter OSSOS detections are consistent with the known populations of the Kuiper belt. The majority of the objects are detected at heliocentric distances  $d$  (top panel) from 28 AU, where the lowest- $q$  resonant TNOs have their perihelia, smoothly out to 40 AU. In the  $d=28-40$  range the inclination distribution is that of the dynamically hot objects; the few low- $i$  objects are the tail of the Gaussian distribution of the dynamically hot objects, down towards  $i=0$ . At  $d \sim 40$  AU there is the sudden appearance of the dynamically cold classical belt. The relative importance of this is muted in our sample due to the relatively shallow depth of the ecliptic 13AE block. Only four of our detections have  $d > 50$  AU.

In  $a/i$  and  $a/e$  space we see the usual spread to large orbital inclinations, predominantly detected in our moderate-latitude 13AO block, and the tail of large- $e$  orbits that correspond to members of the scattering, resonant, and detached populations detected near perihelion. Two resonant objects are the lowest inclination yet found in their resonances: **o3e19** (2013 GR<sub>136</sub>) at  $i = 1.6^\circ$  in the 7:4, and **o3e55** (2013 GX<sub>136</sub>) at  $i = 1.1^\circ$  in the 2:1. In contrast, no such low- $i$  objects exist in the 3:2 plutinos.

Some of the TNOs in the OSSOS discovery sample were previously discovered in other surveys. Seven 13AE and one 13AO object link to “previous discovery” astrometry, either one-night observations from the CFEPS survey, or to objects of varying arc length in the public catalogue at the Minor Planet Center, providing arcs to objects first observed 9 to 13

years ago. Their listings in Table 3 have a “PD” suffix.

The importance of the survey strategy’s emphasis on tracking all objects (§ 2.2) is shown by how it allows us to re-find untracked objects from previous surveys that are on the wrong orbits. For two objects, 2002 GG<sub>166</sub> and 2001 FL<sub>193</sub>, adding our well-sampled arcs extensively modified the orbit from the initial lunation-long arcs: e.g. 2002 GG<sub>166</sub> (o3e01) was initially published<sup>6</sup> as a plutino: here it becomes a Uranus-crossing scattering object (Table 3).

For the other five previously-observed objects, the astrometric quality of the earlier observations were lower than what we report here. Incorporating these earlier observations improved the  $\sigma_a$  of these objects by a factor of only about 2-3 over those of the best 17-month OSSOS orbits. When the OSSOS objects receive MPC designations, the PD objects will thus often get matched to MPC designations with discovery years significantly earlier than 2013 – however, they now benefit from having a well-characterized detection study.

Use of TNO orbits as statistical constraints on models of the formation and evolution of the Solar System is dependent on being certain of the detection characterization of those objects. Often the detected objects below the characterization limit are not well tracked and their inclusion would also contribute ephemeris bias. For OSSOS, the objects whose flux at discovery is below the characterization limit are not included in our model analysis. Those discoveries are listed in Table 4 and have been reported to the MPC.

Over the full  $\sim 170$  deg<sup>2</sup> survey we anticipate detecting  $\sim 500$  outer Solar System objects brightward of our characterization limits. The current rate of detection of TNOs in the OSSOS survey is roughly consistent with expectations given our achieved characterization limits, ecliptic latitude locations surveyed and the currently known luminosity function of TNOs (Fraser et al. 2014). The 13AE discovery rate (49 objects in 21 deg<sup>2</sup>) is somewhat lower than our expected average rate ( $\sim 62$ ) due to the slightly poorer IQ achieved in that part of the survey and the steepness of the TNO luminosity function. Subsequent blocks are being acquired with tighter attention to IQ limits to help ensure the anticipated discovery rate is achieved.

---

<sup>6</sup>MPEC 2002-L21: <http://www.minorplanetcenter.net/mpec/K02/K02L21.html>

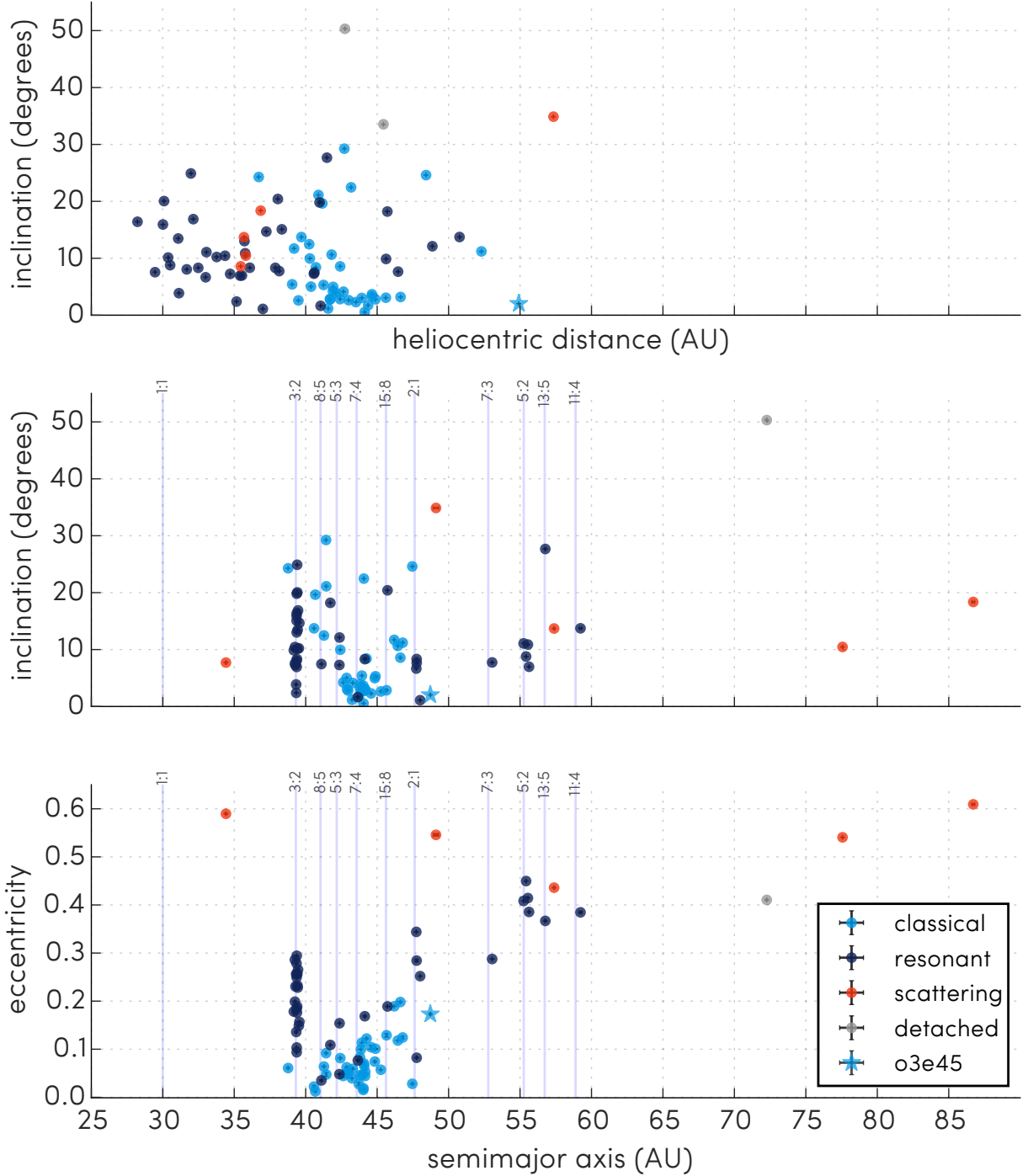


Fig. 12.— Orbital parameters and discovery distances of the 85 characterized OSSOS discoveries (Table 3). o3e01, o3o14, o3e39 are beyond the  $a/e$  and  $a/i$  axes ranges and are excluded from those two sub-plots for clarity. These objects predominantly have orbital arcs of between 353 and 524 days (six have decade-long arcs). The uncertainties are from the covariant matrix fit of Bernstein & Khushalani (2000); note that they are sufficiently small that most error bars are smaller than the point size. o3e45 (2013 GQ<sub>136</sub>) (star), a cold classical beyond the 2:1 resonance with Neptune, is discussed in § 8.2. The pale blue vertical lines show the approximate semi-major axis locations of the resonance centers for resonances

Table 3. Orbit and discovery properties of the characterized OSSOS objects

$m_r$ discovery	$\sigma$ $m_r$ all obs	Eff.	RA (°) discov.	Dec (°) discov.	a (AU)	e	i (°)	d $H$ (AU)	H $r$	MPC design.	Object	Status
Centaur												
23.39(6)	0.17	0.78	239.535	-12.008	22.144(2)	0.37857(6)	32.021(1)	13.77(4)	11.95	2013 JC <sub>64</sub>	o3o01	
23.7(2)	0.34	0.65	216.735	-14.223	38.770(9)	0.061(1)	24.277(1)	36.715(2)	8.0	2013 GO <sub>136</sub>	o3e10	
Inner classical belt												
Main classical belt												
22.97(9)	0.21	0.78	210.435	-10.419	44.10(1)	0.066(2)	2.762(1)	41.714(2)	6.7	2013 GN <sub>137</sub>	o3e22	I
22.99(5)	0.14	0.78	214.785	-11.817	45.259(4)	0.05729(5)	2.633(0)	43.007(1)	6.59	2013 EM <sub>149</sub>	o3e30PD	
23.1(2)	0.23	0.77	214.170	-13.232	43.239(4)	0.03952(6)	1.171(0)	41.569(1)	6.82	2001 FK <sub>185</sub>	o3e20PD	
23.1(1)	0.14	0.77	213.630	-11.944	44.153(4)	0.04422(6)	2.822(0)	42.409(1)	6.77	2004 EU <sub>95</sub>	o3e27PD	
23.2(1)	0.34	0.76	212.175	-11.653	43.294(6)	0.059(1)	4.128(1)	42.647(1)	6.82	2013 GX <sub>137</sub>	o3e28	
23.26(9)	0.31	0.75	216.525	-13.051	47.459(5)	0.028(1)	24.608(2)	48.424(1)	6.34	2013 GG <sub>138</sub>	o3e44	
23.3(2)	0.29	0.74	211.245	-12.982	44.07(3)	0.071(4)	22.463(2)	43.178(4)	6.9	2013 GM <sub>137</sub>	o3e51	
23.37(9)	0.18	0.73	214.845	-13.373	43.963(3)	0.04642(7)	3.316(0)	44.621(1)	6.81	2004 HJ <sub>79</sub>	o3e37PD	
23.37(8)	0.31	0.73	215.040	-11.853	46.447(3)	0.11808(4)	10.63(6)	41.814(1)	7.09	2001 FO <sub>185</sub>	o3e23PD	
23.40(9)	0.23	0.73	213.390	-10.854	45.66(5)	0.129(4)	2.848(1)	41.694(3)	7.12	2013 GQ <sub>137</sub>	o3e21	
23.4(2)	0.18	0.73	235.995	-11.138	40.674(7)	0.0122(8)	19.641(2)	41.166(4)	7.23	2013 JN <sub>65</sub>	o3o28	
23.4(3)	0.35	0.73	214.530	-11.879	43.80(1)	0.083(2)	3.197(1)	46.639(2)	6.67	2013 GV <sub>137</sub>	o3e43	I
23.46(8)	0.21	0.72	211.020	-10.619	41.425(9)	0.092(1)	29.252(1)	42.703(1)	7.09	2013 GO <sub>137</sub>	o3e29	
23.5(1)	0.37	0.72	214.080	-11.197	43.864(5)	0.09974(9)	2.595(1)	39.490(2)	7.44	2013 GS <sub>137</sub>	o3e16	
23.5(1)	0.34	0.71	212.325	-11.247	43.717(8)	0.028(4)	1.748(1)	44.371(2)	6.94	2013 GP <sub>137</sub>	o3e35	
23.5(2)	0.30	0.71	211.530	-12.098	44.884(8)	0.1010(7)	5.309(1)	41.250(1)	7.29	2013 GY <sub>137</sub>	o3e53	
23.5(1)	0.20	0.72	239.085	-12.633	46.20(1)	0.1893(6)	11.707(1)	39.188(1)	7.53	2013 JR <sub>65</sub>	o3o21	
23.5(1)	0.20	0.71	216.015	-11.95	42.89(1)	0.051(3)	3.022(1)	43.926(2)	7.02	2013 GC <sub>138</sub>	o3e32	
23.6(1)	0.26	0.70	214.560	-14.305	44.58(4)	0.104(4)	2.294(2)	43.515(2)	7.1	2013 GT <sub>137</sub>	o3e31	
23.6(1)	0.30	0.70	216.585	-14.088	44.045(4)	0.0187(1)	0.551(0)	44.130(1)	7.05	2013 GF <sub>138</sub>	o3e34PD	
23.59(9)	0.37	0.69	214.710	-13.957	44.837(9)	0.074(1)	4.973(1)	41.922(2)	7.3	2013 GU <sub>137</sub>	o3e25	
23.6(1)	0.21	0.69	215.805	-12.522	42.975(5)	0.0499(6)	2.787(1)	44.882(1)	7.01	2013 GB <sub>138</sub>	o3e38	
23.6(1)	0.24	0.69	211.920	-11.691	42.862(4)	0.0625(3)	5.017(1)	40.370(1)	7.5	2013 GW <sub>137</sub>	o3e54	



Table 3—Continued

$m_r$ discovery	$\sigma m_r$ all obs	Eff.	RA (°) discov.	Dec (°) discov.	a (AU)	e	i (°)	$d_H$ (AU)	$H_r$	MPC design.	Object	Status
23.8(2)	0.27	0.61	216.465	-14.855	44.17(2)	0.053(3)	3.069(2)	45.611(2)	7.16	2013 GE <sub>138</sub>	o3e40	
23.8(1)	0.36	0.61	215.460	-12.938	44.027(9)	0.0153(9)	3.677(2)	44.638(2)	7.3	2013 HT <sub>156</sub>	o3e36	
23.8(2)	0.22	0.60	215.700	-12.322	43.800(4)	0.0458(6)	3.900(1)	42.097(1)	7.52	2013 GA <sub>138</sub>	o3e26	
23.9(1)	0.36	0.58	216.045	-12.328	43.931(5)	0.1136(3)	5.421(1)	39.054(1)	7.87	2013 GD <sub>138</sub>	o3e15	
23.9(4)	0.26	0.58	215.460	-12.182	41.44(2)	0.047(4)	21.117(2)	40.894(2)	7.69	2013 GZ <sub>137</sub>	o3e18	
23.89(9)	0.21	0.68	236.085	-12.921	46.79(2)	0.124(3)	11.206(2)	52.299(4)	6.67	2013 JM <sub>65</sub>	o3o35	
24.0(1)	0.41	0.47	213.885	-12.325	42.63(1)	0.044(4)	4.226(1)	41.903(2)	7.72	2013 GR <sub>137</sub>	o3e24	
24.0(1)	0.14	0.66	236.370	-10.629	41.278(6)	0.0639(9)	12.468(1)	40.245(1)	7.93	2013 JP <sub>65</sub>	o3o23	
24.1(1)	0.20	0.64	238.725	-11.913	44.26(1)	0.122(1)	8.413(0)	40.716(2)	8.0	2013 JQ <sub>65</sub>	o3o26	
24.2(1)	0.19	0.64	241.410	-11.576	40.58(1)	0.022(2)	13.729(1)	39.698(3)	8.12	2013 JS <sub>65</sub>	o3o22	
24.2(1)	0.16	0.63	242.130	-12.475	46.63(3)	0.198(1)	8.573(0)	42.413(2)	7.84	2013 JT <sub>65</sub>	o3o30	
24.4(2)	0.19	0.57	236.085	-10.613	42.42(1)	0.0814(9)	9.958(1)	40.290(2)	8.26	2013 JO <sub>65</sub>	o3o24	
Outer classical belt												
23.6(1)	0.24	0.69	215.070	-13.474	48.72(2)	0.173(2)	2.031(2)	54.915(2)	6.13	2013 GQ <sub>136</sub>	o3e45	
Detached classical belt												
23.07(7)	0.19	0.77	211.890	-11.161	149.8(5)	0.726(1)	33.539(1)	45.442(1)	6.42	2013 GP <sub>136</sub>	o3e39	I
24.4(2)	0.23	0.55	240.510	-11.985	72.26(2)	0.4105(2)	50.318(1)	42.745(2)	8.01	2013 JD <sub>64</sub>	o3o31	
Objects in resonance with Neptune												
22.69(7)	0.22	0.81	216.270	-14.536	47.74(2)	0.3440(4)	6.660(1)	33.001(1)	7.42	2013 GW <sub>136</sub>	o3e05	2:1
23.4(1)	0.36	0.73	211.845	-12.285	48.01(1)	0.2519(5)	1.100(1)	37.002(1)	7.67	2013 GX <sub>136</sub>	o3e55	2:1
23.6(1)	0.15	0.72	236.655	-13.161	47.76(6)	0.284(2)	8.335(1)	36.086(2)	7.94	2013 JE <sub>64</sub>	o3o18	2:1
24.0(1)	0.24	0.67	237.390	-12.517	47.77(1)	0.082(1)	7.65(0)	46.465(2)	7.27	2013 JJ <sub>64</sub>	o3o33	2:1
21.15(2)	0.09	0.85	236.775	-11.987	39.36(5)	0.184(3)	15.081(1)	38.330(2)	5.27	2007 JF <sub>43</sub>	o3o20PD	3:2
23.23(6)	0.13	0.75	237.645	-13.115	39.403(4)	0.18887(8)	24.898(1)	31.965(1)	8.13	2013 JB <sub>65</sub>	o3o09	3:2
23.3(1)	0.21	0.74	213.840	-13.5	39.44(1)	0.2282(7)	13.468(1)	31.080(1)	8.32	2013 GH <sub>137</sub>	o3e02	3:2
23.4(2)	0.27	0.73	214.695	-11.658	39.47(3)	0.265(1)	16.873(1)	32.135(1)	8.25	2013 GJ <sub>137</sub>	o3e04	3:2
23.40(8)	0.16	0.73	240.945	-11.399	39.37(2)	0.2555(9)	19.815(1)	40.970(1)	7.22	2013 JJ <sub>65</sub>	o3o27	3:2
23.48(7)	0.25	0.72	237.360	-11.28	39.371(4)	0.0937(1)	13.015(1)	35.715(1)	7.9	2013 JD <sub>65</sub>	o3o15	3:2

Table 3—Continued

$m_r$ discovery	$\sigma_{m_r}$ all obs	Eff.	RA (°) discov.	Dec (°) discov.	a (AU)	e	i (°)	$d_H$ (AU)	$H_r$	MPC design.	Object	Status
23.62(8)	0.19	0.71	238.020	-12.35	39.363(5)	0.2493(2)	15.934(1)	30.010(1)	8.79	2013 JG <sub>65</sub>	o3o04	3:2
23.67(7)	0.22	0.71	237.225	-11.123	39.375(5)	0.2944(2)	16.409(1)	28.231(1)	9.11	2013 JC <sub>65</sub>	o3o02	3:2
23.69(9)	0.21	0.70	236.145	-10.369	39.419(6)	0.2326(1)	10.12(8)	30.375(1)	8.82	2013 JZ <sub>64</sub>	o3o06	3:2
23.7(1)	0.30	0.65	211.890	-13.064	39.33(3)	0.257(1)	3.866(1)	31.131(1)	8.7	2013 GE <sub>137</sub>	o3e03	3:2
23.9(1)	0.45	0.56	212.805	-12.83	39.56(1)	0.1567(8)	14.680(1)	37.246(1)	8.11	2013 GF <sub>137</sub>	o3e12	3:2
23.9(1)	0.29	0.52	216.690	-13.261	39.17(1)	0.178(1)	9.879(2)	45.625(2)	7.28	2013 GK <sub>137</sub>	o3e41	3:2
24.0(1)	0.23	0.67	239.265	-12.607	39.24(3)	0.286(1)	7.553(0)	29.458(1)	9.22	2013 JH <sub>65</sub>	o3o03	3:2
24.0(1)	0.66	0.45	210.960	-11.526	39.371(5)	0.1035(5)	6.943(1)	35.413(1)	8.45	2013 GD <sub>137</sub>	o3e08	3:2
24.0(3)	0.32	0.44	217.395	-13.633	39.25(3)	0.199(2)	10.440(1)	34.356(1)	8.59	2013 GL <sub>137</sub>	o3e06	3:2
24.1(2)	0.33	0.41	212.640	-10.849	39.34(2)	0.136(2)	2.391(1)	35.160(1)	8.52	2013 GG <sub>137</sub>	o3e07	3:2
24.1(1)	0.21	0.65	238.605	-13.216	39.389(4)	0.1762(1)	8.316(0)	32.482(1)	8.94	2013 JF <sub>65</sub>	o3o10	3:2
24.1(2)	0.18	0.65	236.910	-10.624	39.520(5)	0.1488(2)	10.223(0)	33.771(1)	8.78	2013 JA <sub>65</sub>	o3o12	3:2
24.2(1)	0.20	0.63	238.305	-13.255	39.358(9)	0.2784(4)	8.048(0)	31.676(1)	9.15	2013 JE <sub>65</sub>	o3o08	3:2
24.3(1)	0.28	0.61	243.045	-13.607	39.29(1)	0.2306(7)	7.251(0)	34.714(1)	8.79	2013 JL <sub>65</sub>	o3o13	3:2
24.3(1)	0.24	0.60	241.455	-12.778	39.416(6)	0.2566(2)	20.045(1)	30.089(1)	9.44	2013 JK <sub>65</sub>	o3o05	3:2
22.94(4)	0.17	0.77	238.425	-12.45	55.250(9)	0.4083(1)	11.077(0)	33.054(1)	7.69	2013 JK <sub>64</sub>	o3o11	5:2
22.94(5)	0.19	0.79	216.855	-15.028	55.55(3)	0.4143(5)	10.877(1)	35.765(1)	7.32	2013 GY <sub>136</sub>	o3e09	5:2
23.9(3)	0.20	0.68	236.805	-12.989	55.42(1)	0.44971(9)	8.785(0)	30.514(1)	8.97	2013 JF <sub>64</sub>	o3o07	5:2
23.9(2)	0.27	0.54	210.480	-10.686	55.63(3)	0.3855(6)	6.978(1)	35.539(2)	8.34	2013 GS <sub>136</sub>	o3e48	5:2
24.1(2)	0.22	0.40	211.260	-10.733	42.370(4)	0.1540(2)	12.112(2)	48.863(2)	7.11	2013 GT <sub>136</sub>	o3e52	5:3 IH
24.1(1)	0.29	0.64	242.025	-13.547	42.358(5)	0.0481(5)	7.287(0)	40.573(1)	7.98	2013 JM <sub>64</sub>	o3o25	5:3 I
23.8(2)	0.24	0.69	242.010	-12.902	53.05(1)	0.2876(3)	7.74(0)	38.148(1)	7.96	2013 JN <sub>64</sub>	o3o19	7:3
23.4(1)	0.35	0.73	211.185	-12.217	43.649(7)	0.0767(7)	1.645(1)	41.043(1)	7.2	2013 GR <sub>136</sub>	o3e19	7:4
24.0(1)	0.20	0.47	214.920	-13.83	41.100(6)	0.035(1)	7.452(1)	40.609(1)	7.85	2013 GV <sub>136</sub>	o3e17	8:5 IH
22.70(4)	0.11	0.79	237.195	-13.113	59.23(8)	0.385(2)	13.731(1)	50.766(2)	5.6	2013 JH <sub>64</sub>	o3o34	11:4 I
23.3(1)	0.23	0.75	238.815	-12.604	56.77(5)	0.367(1)	27.672(1)	41.487(1)	7.03	2013 JL <sub>64</sub>	o3o29	13:5 IH
23.54(9)	0.22	0.70	215.355	-12.892	45.73(1)	0.1889(5)	20.412(1)	38.052(1)	7.72	2013 HR <sub>156</sub>	o3e49	15:8 I
23.7(1)	0.31	0.65	212.220	-10.496	44.14(2)	0.169(1)	8.318(1)	37.876(1)	7.86	2013 GU <sub>136</sub>	o3e13	16:9 IH
24.1(1)	0.20	0.64	236.670	-10.521	41.725(7)	0.1088(7)	18.208(1)	45.715(2)	7.48	2013 JG <sub>64</sub>	o3o32	18:11 IH
Scattering disk												
21.50(9)	0.18	0.88	213.150	-13.587	34.42(4)	0.5897(6)	7.711(1)	23.291(1)	7.73	2002 GG <sub>166</sub>	o3e01	
23.54(8)	0.17	0.72	237.030	-12.827	143.31(9)	0.7548(2)	8.58(0)	35.456(1)	8.0	2013 JO <sub>64</sub>	o3o14	

Table 3—Continued

$m_r$ discovery	$\sigma$ $m_r$ all obs	Eff.	RA (°) discov.	Dec (°) discov.	$a$ (AU)	$e$	$i$ (°)	$d_H$ (AU)	$H_r$	MPC design.	Object	Status
23.6(1)	0.65	0.69	210.615	-12.965	86.72(9)	0.6092(5)	18.363(1)	36.851(1)	7.86	2013 GZ <sub>136</sub>	o3e11	
23.73(9)	0.17	0.70	241.740	-14.215	49.1(2)	0.546(3)	34.876(4)	57.339(6)	6.09	2013 JQ <sub>64</sub>	o3o36	I
23.9(1)	0.15	0.68	239.805	-12.537	57.38(4)	0.4359(6)	13.701(1)	35.680(1)	8.34	2013 JP <sub>64</sub>	o3o16	
24.3(1)	0.32	0.59	241.440	-12.657	77.57(2)	0.5406(2)	10.459(1)	35.811(1)	8.71	2013 JR <sub>64</sub>	o3o17	

Note. — Numbers in parentheses are the uncertainty in the last given digit.  $m_r$  discovery is an average magnitude during the discovery triplet only, eliding any measurements with photometric flags.  $\sigma$   $m_r$  is the standard deviation of all measured magnitudes without photometric flags. Eff. is the value of the detection efficiency function for the motion rate of the object at its discovery.  $a$ ,  $e$ ,  $i$  are J2000 ecliptic barycentric coordinates of semi-major axis, eccentricity, inclination, with uncertainties from the covariant matrix fit of Bernstein & Kushalani (2000); full barycentric elements are available at <http://www.ossos-survey.org/>. The full heliocentric orbital elements are available in electronic form from the Minor Planet Center. We assign survey designations here based on their OSSOS discovery, with a format  $o$  for OSSOS, the last digit of the year in which the object was discovered by OSSOS (3-6), the block ID letter ( $e$ ,  $o$ ) and the sequential number 01-xx to give unique identifiers.  $p$  :  $q$ : object is in the  $p$  :  $q$  resonance; I: the orbit classification is currently insecure; H: the human operator intervened to declare the orbit security status.

Table 4. Orbit and discovery properties of the uncharacterized OSSOS objects

$m_r$ discovery	$\sigma m_r$ all obs	Eff.	RA (°) discov.	Dec (°) discov.	a (AU)	e	i (°)	$d_H$ (AU)	$H_r$	MPC design.	Object
Arc outside discovery lunation (via serendipitous tracking observations)											
24.1(1)	0.21	0.35	215.790	-13.635	45.65(4)	0.176(2)	8.261(1)	38.536(3)	8.23	2013 HS <sub>156</sub>	uo3e14
24.3(2)	0.44	0.15	214.380	-13.558	43.22(1)	0.024(3)	2.308(2)	43.812(2)	7.81	2013 GC <sub>137</sub>	uo3e33
24.5(2)	0.26	0.45	237.615	-11.245	40.179(9)	0.0702(6)	26.609(3)	37.372(3)	8.72	2013 JU <sub>64</sub>	uo3o37
24.5(3)	0.25	0.43	236.640	-12.721	42.527(8)	0.049(8)	9.633(2)	40.645(5)	8.39	2013 JS <sub>64</sub>	uo3o38
24.6(2)	0.31	0.36	238.125	-11.727	73.0(7)	0.575(6)	31.388(2)	53.286(3)	7.26	2013 JV <sub>64</sub>	uo3o50
Arc only within discovery lunation											
24.2(2)	0.29	0.27	212.565	-11.181	43(22)	0.0(6)	12.2(4.7)	42.2(2.7)	7.85		uo3e50nt
24.4(1)	0.05	0.55	240.285	-13.07	44(23)	0.0(6)	27(26)	43.0(5.1)	8.0		uo3o46nt
24.4(2)	0.02	0.53	237.975	-11.892	38(20)	0.0(6)	9.6(9)	37.4(2.4)	8.64		uo3o43nt
24.5(2)	0.23	0.46	241.665	-12.826	35(19)	0.0(6)	11.2(1.9)	34.3(2.5)	9.07		uo3o39nt
24.5(2)	0.10	0.45	237.300	-12.453	42(22)	0.0(6)	23(24)	41.3(4.9)	8.29		uo3o47nt
24.5(2)	0.25	0.04	212.340	-10.629	50(25)	0.3(5)	2.6(1)	44.7(1.3)	7.93		uo3e42
24.5(2)	0.17	0.44	241.350	-13.576	36(19)	0.0(6)	11(13)	35.1(3.7)	9.0		uo3o40nt
24.5(2)	0.19	0.44	241.650	-13.872	38(20)	0.0(6)	9(12)	37.1(3.9)	8.75		uo3o42nt
24.6(2)	0.26	0.01	213.645	-11.146	16(12)	0.1(9)	32(32)	14.5(4.6)	12.88		uo3e46nt
24.6(2)	0.14	0.34	241.800	-13.145	37(20)	0.0(6)	9.0(9)	36.0(2.5)	8.96		uo3o41nt
24.7(2)	–	0.23	238.695	-11.017	40(21)	0.0(6)	8.9(1.9)	38.7(4.1)	8.74		uo3o44nt
24.7(2)	0.23	0.19	242.460	-13.232	44(23)	0.0(6)	7.8(5)	42.7(2.6)	8.33		uo3o45nt
24.7(2)	–	0.19	237.000	-12.451	47(25)	0.0(6)	40(49)	46.5(8.4)	7.98		uo3o48nt
24.8(3)	–	0.11	236.865	-10.903	49(25)	0.0(6)	8.9(6.2)	48.4(5.5)	7.89		uo3o49nt

Note. — Serendipitous tracking observations are those where the object happened to be within and was visible in images taken to extend the orbital arc of characterized OSSOS objects. Numbers in parentheses are the uncertainty in the last given digit.  $m_r$  discovery is an average magnitude during the discovery triplet only, eliding any measurements with photometric flags.  $\sigma m_r$  is the standard deviation of all measured magnitudes without photometric flags. Eff. is the value of the detection efficiency function for the motion rate of the object at its discovery.  $a, e, i$  are J2000 ecliptic barycentric coordinates of semi-major axis, eccentricity, inclination, with uncertainties from the covariant matrix fit of Bernstein & Khushalani (2000); full barycentric elements are available at <http://www.ossos-survey.org/>. The full heliocentric orbital elements are available in electronic form

from the Minor Planet Center. We assign survey designations here based on their OSSOS discovery, with a format  $o$  for OSSOS, the last digit of the year in which the object was discovered by OSSOS (3-6), the block ID letter ( $e, o$ ) and the sequential number 01-xx to give unique identifiers. Orbital classifications are not applied to these objects. “u” indicates uncharacterized; “nt” at the end of the object ID designates not observed on more than two nights in the discovery lunation.

## 8. Substructure of the classical belt

Petit et al. (2011) noted the need for substructure in the main classical belt: the population with semimajor axes between the 3:2 and 2:1 mean-motion resonances with Neptune, considering only  $40 \leq a \leq 47$  AU to avoid the complex resonance boundaries around 39.4 and 47.8 AU respectively. That work showed that the main classical belt could be modelled with three components within  $a/e/i$  phase space (hereafter: the CFEPS *L7 model*; see Fig. 4 and Appendix A in Petit et al. (2011)). With the first OSSOS sample, we confirm this three-component view (Fig. 13).

The dynamically excited hot classical belt is described by a single smooth *hot component*: widely distributed with width  $\sigma_h = 16^\circ$  in inclination, continuously covering all stable semimajor axes  $a$  beyond Neptune, with a hole scooped out  $i < 12^\circ$ ,  $a < 42.4$  AU to account for the destabilizing action of the  $\nu_8$  secular resonance (Fig. 13, lower left, lightest grey points). In contrast, the cold classical belt forms a low-inclination narrow band (Fig. 13, lower left, darker grey points) with inclination width of roughly  $2^\circ$ , described by the superposition of two components (discussed in detail below, § 8.1). The cold belt begins beyond  $a = 42.5$  AU and forms a low-eccentricity clump around 44 AU (Fig. 13, lower right). Considering the perihelion distribution in the main classical belt, we also confirm the difference in the perihelion distribution of the hot and cold main-belt populations seen by Petit et al. (2011) (Fig. 13, upper right). The hot population seen by OSSOS is concentrated in the perihelion range  $q = 35 - 41$  AU, with soft exponential decay about an AU to either side, while the cold belt population has perihelia 38–47 AU (Fig. 13).

Interior to the main belt, the inner classical belt objects inhabit a more limited stable phase space due to the  $\nu_8$  secular resonance; they comprise the non-resonant, non-scattering population  $a_{Neptune} < a < 3:2$  mean-motion resonance. Inner belt objects detected in previous surveys in the  $a = 34-39$  AU range are consistent with being detections of the low- $a$  tail of the main belt hot population (Petit et al. 2011). Photometric studies support this through colours more consistent with those of the hot main-belt population rather than the distinctly red cold classicals (Peixinho et al. 2015; Romanishin et al. 2010). The lone OSSOS detection in the inner classical belt, **o3e10**, has  $i = 24^\circ$  (Fig. 13, lower left). The sample therefore remains consistent with the inner classical belt being a lower- $a$  tail of the hot main belt.

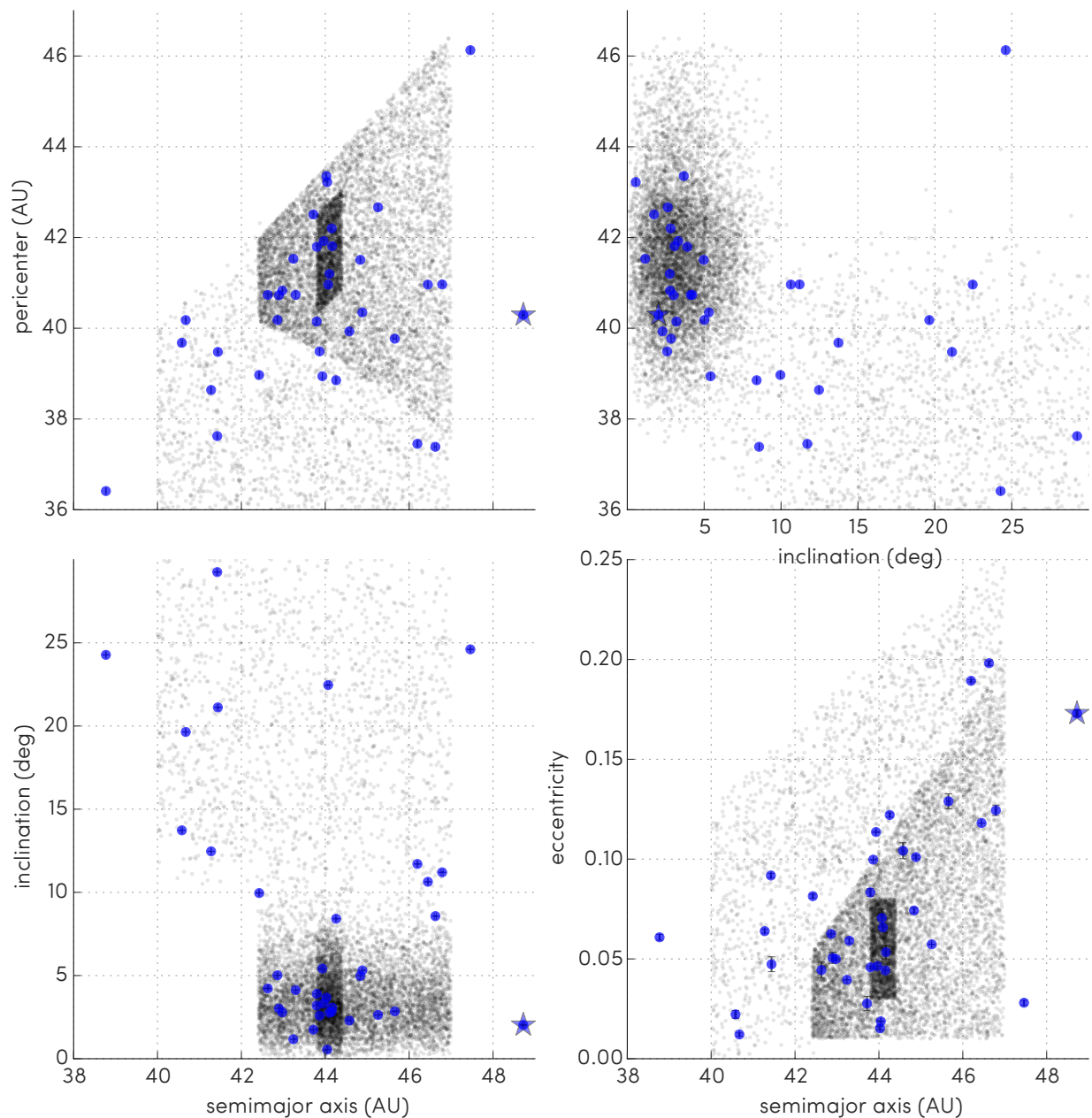


Fig. 13.— Orbital parameters of the characterized OSSOS discoveries classified within the classical belt (Table 3; blue points); outer classical belt object o3e45 (star) is discussed in § 8.2. Backgrounded in greys is the inferred three-component model of the intrinsic classical belt population built in the 40-47 AU region between the 3:2 and 2:1 resonances, § 8: lightest grey is the dynamically excited hot component, mid grey and dark grey the two components of the cold main belt, stirred (mid grey) and the kernel (darkest grey). The perihelion distribution of the hot and cold populations can be clearly distinguished (top right plot). The uncertainties to the orbital parameters of the OSSOS discoveries are from the covariant matrix fit of Bernstein & Khushalani (2000); note that they are sufficiently small that most error bars are smaller than the point size.

### 8.1. A kernel exists in the cold classical belt

One of the important findings of Petit et al. (2011) is the substructure present in the cold component of the main classical belt. Is this structure also present in the OSSOS first-quarter sample, or did Petit et al. (2011) over-interpret a fluctuation in their data?

Petit et al. (2011) represented this substructure in their L7 model by two superposed components. A small *kernel component* compact in  $a$  and  $i$  was centered near 44 AU. Overlaying this was a population that at some time was slightly dynamically agitated by weak interactions, the *stirred component*, which is smooth in semi-major axis distribution, cold in inclination and occupies  $q = 38\text{--}44$  AU with  $a = 42.4\text{--}47$  AU. The stirred component’s inner edge begins at the  $\nu_8$  secular resonance and the outer bound is the 2:1 mean-motion resonance. The split to two components was informed by the clumped,  $a$ -dependent nature of the  $e$  distribution. Fig. 12 and Fig. 13 show that indeed the over-density near  $a = 44$  AU is also present in the OSSOS discoveries.

However, to prove that Petit et al. (2011) did not over-interpret the previous detections, we tested the detected OSSOS  $a$  distribution in turn against a smooth distribution and against the L7 model of the classical belt substructure (Fig. 14), using the same Anderson-Darling tests<sup>7</sup> for the  $a$  distribution as were done by Petit et al. (2011). The data demand a substructure in the cold component: a model using only a smooth  $a$  distribution for the cold component, with no kernel, was rejected at more than 95% confidence by the OSSOS detections. We therefore confirm that there is a real “kernel” concentration in the Kuiper belt in the narrow semi-major axis range around 44 AU.

While it is plausible that other two-component models might be used to represent the classical belt, the L7 model at present still provides a valid representation of the orbital distribution for the main-belt’s cold component: it could not be rejected by the OSSOS sample at the 80% confidence level (Fig. 14).

### 8.2. A stirred tail of cold classicals beyond the 2:1 resonance?

The first-quarter OSSOS sample includes the newly discovered object **o3e45** (2013 GQ<sub>136</sub>), which has  $a = 48.72$  AU,  $e = 0.173$ , and  $i = 2.031^\circ$ . With  $q = 40.3$  AU (Fig. 13), this object lies along a natural extension of the stirred component. Crucially, its orbit is beyond the current barrier of the 2:1 resonance (Fig 12). Is this object part of the smoothly  $a$ -distributed

---

<sup>7</sup><http://www.itl.nist.gov/div898/handbook/eda/section3/eda35e.htm>



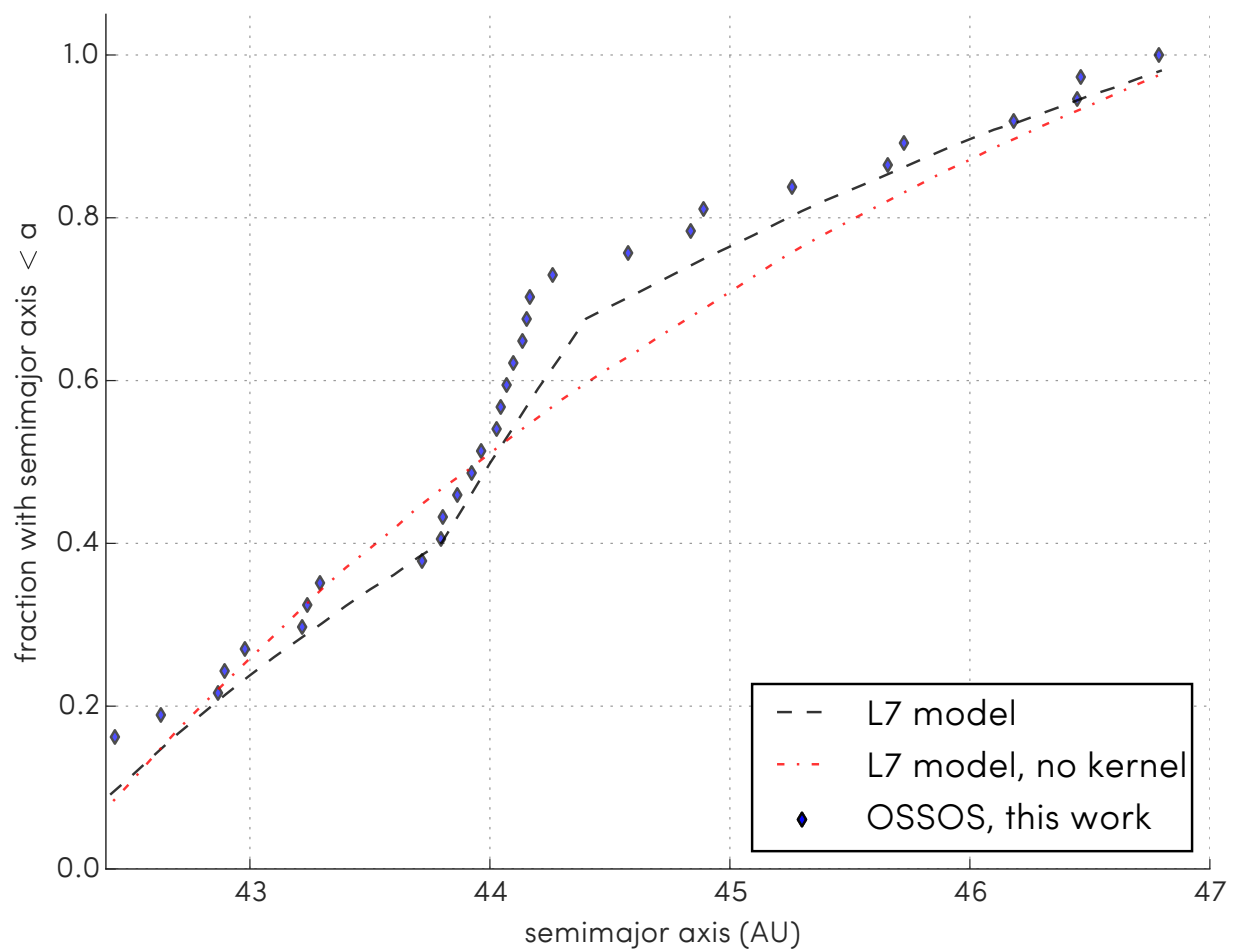


Fig. 14.— Cumulative semi-major axis distribution of the first-quarter OSSOS main-belt detections (diamonds). The dashed curve shows the cumulative distribution of the expected detections if the CFEPS L7 model of Petit et al. (2011) is biased through the OSSOS survey simulator. This model reasonably predicts the high density of OSSOS detections near 44 AU, via a ‘kernel’ subcomponent in the model. Removing the kernel and simulating the main-belt detections with a cold component that is instead purely smooth produces a predicted semi-major axis distribution for the detections (dotted line) that is rejected at more than 95% tolerance.

‘stirred’ component that we modelled in the cold main belt? If so, this would have strong cosmogonic implications.

**o3e45** joins only two other published objects with low- $i$  objects just beyond the 2:1 resonance: 2003 UY<sub>291</sub> (Gladman et al. 2008), with  $a = 49.4$  AU,  $e = 0.16$ ,  $i = 3.5^\circ$ , and the newly recovered<sup>8</sup> 2001 FL<sub>193</sub>, with  $a = 50.17$  AU,  $e = 0.20$ ,  $i = 1.0^\circ$ .

These objects could imply a scenario where present  $a > 44.5$  AU members of the stirred component are objects shifted from a primordial  $a < 44.5$  AU ( $a$  beyond the outer edge of the kernel). In a past where Neptune’s eccentricity was larger than at present, these objects were stirred by weak close encounters, sufficiently gentle that their eccentricities minimally modified, out into a scattered tail. Could there now be a continuous distribution of primordial cold objects, scattered from initial locations in the 40–42 AU distance range where the kernel perihelia centre, that presently are on orbits with perihelia at their original position? This could require cosmogonic models to scatter cold objects into an extended belt beyond the 2:1 resonance while creating or preserving a concentration of the same cold objects at  $a \sim 44$  AU.

We confirmed in § 8.1 that the L7 model is a reasonable match to the OSSOS main classical Kuiper belt detections. The main classical Kuiper belt lies by definition between the 3:2 and 2:1 resonances. The L7 model of the cold main classical therefore has a maximum semi-major axis placed at the 2:1 resonance, at 47 AU. The overall L7 model did not have an ‘outer’ cold main classical Kuiper belt beyond 47 AU, as the hot classical component of the L7 model sufficiently explained the CFEPS detections. Does the stirred component of the L7 model of the cold main classical extend into the outer classical belt?

If we smoothly extend the stirred component of the CFEPS L7 model, how many detections with OSSOS do we predict? We used the same population  $P(a) \propto a^{-2.5}$  distribution as in Petit et al. (2011) (Appendix A) and in § 8. The  $q$  distribution of the component was allowed to be wider than in the L7 model, going from 38 AU to the  $a$  value being tested. The centre of the 2:1 resonance is 47.7 AU, with a width  $\pm 0.4$  AU; we therefore excluded component  $q$  values that occurred in the 47.4–48.2 region. The detection of one low- $i$ ,  $a > 47$  AU object, as we found in this survey (**o3e45**), is consistent with a stirred component smoothly extending to at least 49 AU.

---

<sup>8</sup> 2001 FL<sub>193</sub> on its discovery in 2001 (MPEC 2001-U19: <http://www.minorplanetcenter.net/mpec/K01/K01U19.html>) was assigned to an  $a = 44$  AU,  $e = 0.09$  orbit and subsequently lost. Its June 2015 recovery and orbit revision (MPEC 2015-M50: <http://www.minorplanetcenter.net/mpec/K15/K15M50.html>) showed it actually has  $a = 50.2$  AU,  $e = 0.20$ . This echoes the perils of ephemeris bias (Jones et al. 2010).

The further the stirred component extends, the higher the number of low- $i$ ,  $a > 47$  AU detections that should be made by OSSOS. Extending this component further to 60 AU would imply 5 low- $i$ ,  $a > 47$  AU detections by OSSOS. (This continues to hold, though at the 92% confidence level, if the test is instead made with the power law of the distribution steepened up to  $P(a) \propto a^{-4.5}$ ). As we have only one such OSSOS detection, we reject a stirred component extending beyond 60 AU at the 95% confidence level, under the assumption that the smooth extension is a power law.

The alternate hypothesis is that o3e45 and the two previously discovered low- $i$ ,  $a > 47$  AU objects are simply the low- $i$  tail of the hot population of the main Kuiper belt. o3e45 has a low probability of being a member of this hot component. The CFEPS L7 model predicts that the 13A OSSOS blocks have just 5% probability of detecting one or more hot component objects in the  $a > 47.5$  AU,  $i < 5^\circ$ ,  $q > 40$  zone, where we have one detection. Further detections of objects in this zone of orbit parameter space are needed before more conclusive statements can be made. These will depend on the abundance of such objects in future OSSOS blocks relative to the abundance of the hot population, and on how low their  $a$  and  $e$  may be, but three to four detections would help.

## 9. Conclusion

From the first quarter of the Outer Solar System Origins Survey (OSSOS), discovered in 2013 and tracked 2013-2014 exclusively with CFHT’s MegaPrime wide-field imager, we report 85 discovered objects from two 21-deg<sup>2</sup> blocks of sky: 49 objects in block 13AE to a characterized depth of  $m_r = 24.09$  and 36 objects in block 13AO to a characterized depth of  $m_r = 24.40$ . These comprise 1 centaur, 39 resonant objects, 40 classical objects, 3 detached objects, and 6 scattering objects, as classified according to the nomenclature and technique of Gladman et al. (2008).

This sample is without ephemeris bias, as it is 100% tracked above the characterization magnitude, a first for large surveys of the Kuiper belt. The orbital elements of the discoveries are precise to at minimum  $\sigma_a < 1\%$ , with most precise to  $\sigma_a < 0.1\%$  after 12–17-month arcs. This accuracy was achieved in a significantly shorter period than in previous surveys, thanks to the internally consistent astrometric catalogue and increased observing cadence. These 85 objects can immediately be folded into the known objects usable for testing models of Solar System architecture evolution, via our survey simulator.

This initial OSSOS detected sample confirms the existence of substructure within the main classical Kuiper belt, as first reported in Petit et al. (2011). We find that the semi-

major axis distribution of the stirred component of the cold classicals cannot have a smooth distribution: it must contain a ‘kernel’. There appears also to be a tail of cold classical objects stirred out beyond the 2:1 resonance that extends to at least 50 AU. Its extent beyond that is as yet unclear.

*Facilities:* CFHT (MegaPrime).

This research was supported by funding from the National Research Council of Canada and the National Science and Engineering Research Council of Canada. This project could not have been a success without the dedicated staff of the Canada-France-Hawaii telescope. The authors recognize and acknowledge the sacred nature of Maunakea, and appreciate the opportunity to observe from the mountain. This research has made use of NASA’s Astrophysics Data System, GNU `parallel` (Tange 2011), and many Python packages, particularly `astropy` (The Astropy Collaboration et al. 2013), `matplotlib` (Hunter 2007) and `SciPy` (Jones et al. 2001); we thank their contributors for their open-source efforts. MES is supported in part by an Academia Sinica Postdoctoral Fellowship. Based on observations obtained with MegaPrime/MegaCam, a joint project of the Canada–France–Hawaii Telescope (CFHT) and CEA/DAPNIA, at CFHT which is operated by the National Research Council (NRC) of Canada, the Institut National des Sciences de l’Univers of the Centre National de la Recherche Scientifique (CNRS) of France, and the University of Hawaii. This work is based in part on data produced and hosted at the Canadian Astronomy Data Centre.

## 10. Availability

Existing development and source code is available for contribution and for download by the public from GitHub (the data pipeline at <https://github.com/OSSOS/MOP>, and the Survey Simulator at <https://github.com/OSSOS/SurveySimulator>). Versions of the figures suitable for use in presentations are at <https://github.com/OSSOS/Publications>.

## 11. Appendix A

Contrary to deep stellar or galactic surveys which analyze stacked images, moving object surveys rely on detecting the source on each and every single image of the discovery triplet. For a given intrinsic magnitude, an object can appear brighter or dimmer due to Poisson fluctuations of the source itself and of the background. Thus the measured magnitude scatters around the intrinsic value. For objects much brighter than the detection limit, the

scatter is small in relative value, but it becomes important close to the limit. This scatter produces an asymmetry in the magnitude of measured objects: objects whose magnitudes scatter up will be easier to detect and preferentially retained, while those that scatter down will be too dim to be detected (Malmquist bias). This effect can be seen in Fig. 15. At the faint end, we clearly see the asymmetry with more objects having a lower apparent magnitude, i.e. brighter, than the intrinsic magnitude.

For the OSSOS simulator, the statistics of measured apparent magnitude versus intrinsic magnitude determined here also allows us to simulate the scatter and apply it to the intrinsic magnitude of the model objects to obtain a simulated measured magnitude. This is the magnitude that will be used to compare with the real detections. To decrease the RMS of the magnitude uncertainty, creating less noise in the determination of the slope and consequently on the population estimate error, we took the mean magnitude of the object on the discovery triplet as the defining magnitude of the object that we place in the simulator for comparison to the simulated detections. If one or more of the triplet’s sources was not appropriate for photometry, e.g. due to involvement with a star or galaxy, we excluded it from this mean. Out of the 85 objects in the characterized sample from the 13AE and 13AO blocks, 2 objects had only one useful photometric measurement and 12 objects had only two. For each simulated detection, we determine the mean and standard deviation of the magnitude scatter, following the trends determined on the fake implanted objects (see Fig. 16), and draw a Gaussian distributed random number with these parameters. This yields a simulated measured magnitude. We repeat this procedure 1, 2 or 3 times following the frequency determined on the real/fake detections. We finally average the simulated measured magnitudes to obtain the surmised magnitude which will be compared to the average magnitude of the real detections.

## REFERENCES

- Ahn, C. P., Alexandroff, R., Allende Prieto, C., et al. 2014, *The Astrophysical Journal Supplement Series*, 211, 17
- Alexandersen, M., Gladman, B., Kavelaars, J. J., et al. 2014, arXiv.org, 1411.7953v1
- Bannister, M. T. in press, 2015, *Planetary and Space Science*
- Bernstein, G., & Khushalani, B. 2000, *The Astronomical Journal*, 120, 3323
- Bernstein, G. M., Trilling, D. E., Allen, R. L., et al. 2004, *The Astronomical Journal*, 128, 1364

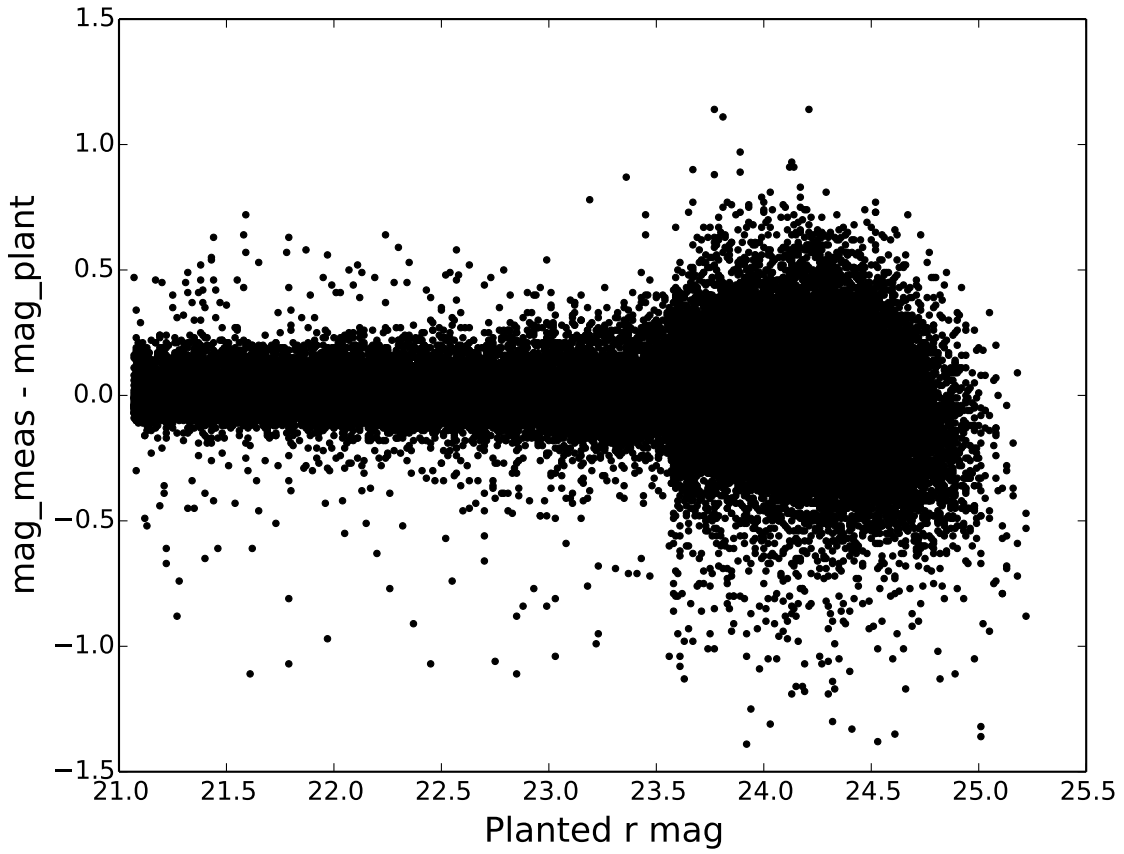


Fig. 15.— Difference of measured magnitude from intrinsic magnitude for all fake objects implanted in the 13AO block to determine the detection efficiency.

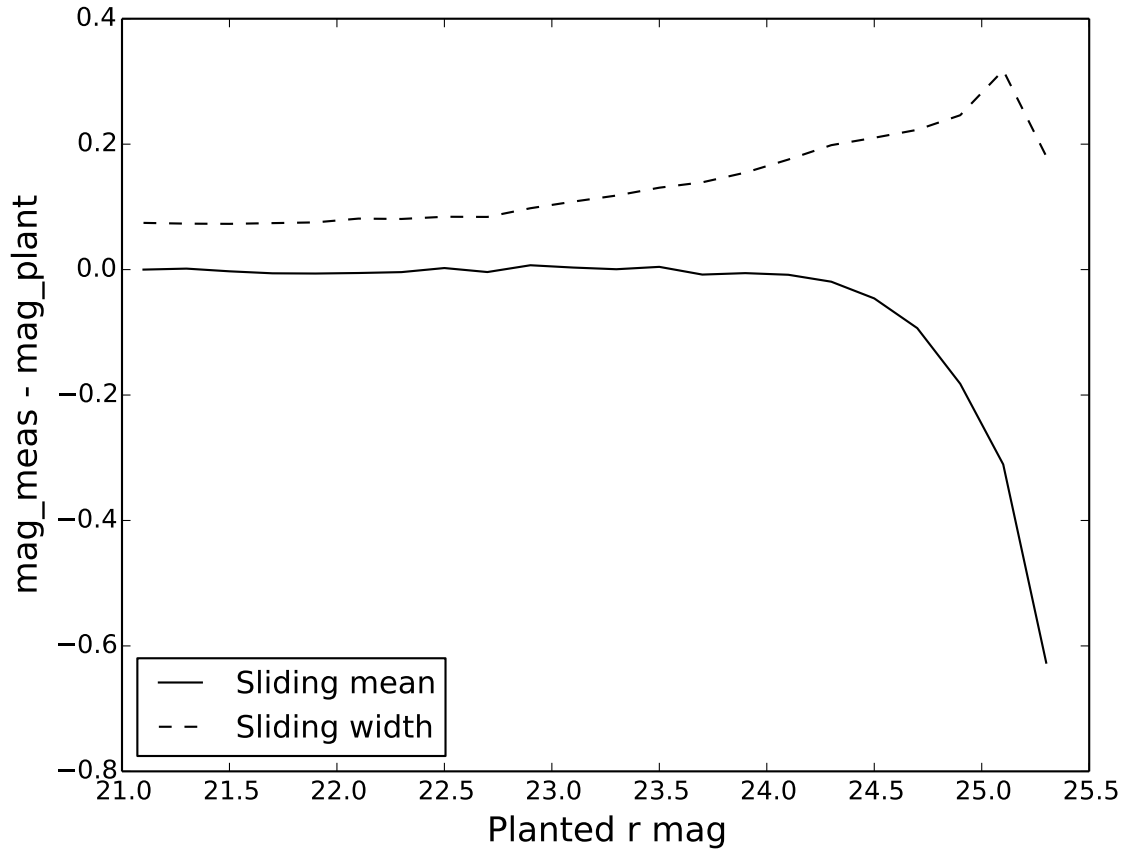


Fig. 16.— Mean (solid line) and standard deviation (dashed line) of measured magnitude minus intrinsic magnitude versus intrinsic magnitudes for all implanted objects in the 13AO block. Mean and standard deviation have been evaluated on 0.2 magnitude bins, with iterative rejection of points beyond  $3\text{-}\sigma$ .

- Bertin, E., & Arnouts, S. 1996, *Astronomy and Astrophysics Supplement*, 117, 393
- Boulade, O., Charlot, X., Abbon, P., et al. 2003, *Instrument Design and Performance for Optical/Infrared Ground-based Telescopes*. Edited by Iye, 4841, 72
- Brown, M. E., & Pan, M. 2004, *The Astronomical Journal*, 127, 2418
- Chiang, E., & Choi, H. 2008, *Astronomical Journal*, 136, 350
- Collander-Brown, S. 2003, *Icarus*, 162, 22
- Elliot, J. L., Kern, S. D., Clancy, K. B., et al. 2005, *The Astronomical Journal*, 129, 1117
- Fernandez, J. A., & Ip, W. H. 1984, *Icarus*, 58, 109
- Fraser, W. C. 2009, *Astrophysical Journal*, 119
- Fraser, W. C., Brown, M. E., Morbidelli, A., Parker, A., & Batygin, K. 2014, *The Astrophysical Journal*, 782, 100
- Fraser, W. C., & Kavelaars, J. J. 2009, *The Astronomical Journal*, 137, 72
- Fuentes, C. I., George, M. R., & Holman, M. J. 2009, *The Astrophysical Journal*, 696, 91
- Giorgini, J. D., Yeomans, D. K., Chamberlin, A. B., et al. 1996, in *Bulletin of the American Astronomical Society*, Vol. 28, *Bulletin of the American Astronomical Society*, 1158
- Gladman, B., Kavelaars, J. J., Nicholson, P. D., Loredo, T. J., & Burns, J. A. 1998, *The Astronomical Journal*, 116, 2042
- Gladman, B., Marsden, B. G., & Vanlaerhoven, C. 2008, in *The Solar System Beyond Neptune*, ed. M. A. Barucci, H. Boehnhardt, D. P. Cruikshank, A. Morbidelli, & R. Dotson (The University of Arizona Press), 43–57
- Gladman, B., Lawler, S. M., Petit, J.-M., et al. 2012, *The Astronomical Journal*, 144, 23
- Gladman, B. J., Davis, D. R., Neese, C., et al. 2009, *ICARUS*, 202, 104
- Gwyn, S. D. J. 2008, *Publications of the Astronomical Society of the Pacific*, 120, 212
- . 2014, *Journal of Instrumentation*, 9, C04003
- Gwyn, S. D. J., Hill, N., & Kavelaars, J. J. 2012, *Publications of the Astronomical Society of the Pacific*, 124, 579



- Hahn, J. M., & Malhotra, R. 1999, *The Astronomical Journal*, 117, 3041
- . 2005, *The Astronomical Journal*, 130, 2392
- Hainaut, O. R., Boehnhardt, H., & Protopapa, S. 2012, *Astronomy and Astrophysics*, 546, A115
- Hunter, J. D. 2007, *Computing In Science & Engineering*, 9, 90
- Jones, E., Oliphant, T., Peterson, P., & Others. 2001, *SciPy: Open source scientific tools for Python*
- Jones, R. L., Parker, J. W., Bieryla, A., et al. 2010, *The Astronomical Journal*, 139, 2249
- Jones, R. L., Gladman, B., Petit, J.-M., et al. 2006, *ICARUS*, 185, 508
- Kavelaars, J. 2013, in *Astronomical Data Analysis Software and Systems XXII. Proceedings of a Conference held at University of Illinois*, 243
- Kavelaars, J., Jones, L., Gladman, B., Parker, J. W., & Petit, J.-M. 2008, in *The Solar System Beyond Neptune*, ed. M. A. Barucci, H. Boehnhardt, D. P. Cruikshank, A. Morbidelli, & R. Dotson (University of Arizona Press, Tucson), 59–69
- Kavelaars, J. J., Jones, R. L., Gladman, B. J., et al. 2009, *The Astronomical Journal*, 137, 4917
- Kenyon, S. J., & Bromley, B. C. 2008, *The Astrophysical Journal Supplement Series*, 179, 451
- Lawler, S. M., & Gladman, B. 2013, *The Astronomical Journal*, 146, 6
- Levison, H. F., & Duncan, M. J. 1994, *ICARUS*, 108, 18
- Levison, H. F., Morbidelli, A., Vanlaerhoven, C., Gomes, R., & Tsiganis, K. 2008, *ICARUS*, 196, 258
- Luu, J. X., & Jewitt, D. 1988, *The Astronomical Journal*, 95, 1256
- Malhotra, R. 1995, *The Astronomical Journal*, 110, 420
- Millis, R. L., Buie, M. W., Wasserman, L. H., et al. 2002, *The Astronomical Journal*, 123, 2083
- Mommert, M., Harris, A. W., Kiss, C., et al. 2012, *Astronomy and Astrophysics*, 541, A93

- Murray-Clay, R. A., & Chiang, E. I. 2005, *The Astrophysical Journal*, astro-ph, 623
- Nesvorny, D. 2015, arXiv.org, 6021
- Ochsenbein, F., Bauer, P., & Marcout, J. 2000, *Astronomy and Astrophysics Supplement Series*, 143, 23
- Peixinho, N., Delsanti, A., & Doressoundiram, A. 2015, *Astronomy and Astrophysics*, 577, A35
- Petit, J.-M., Holman, M., Scholl, H., Kavelaars, J., & Gladman, B. 2004, *Monthly Notices of the Royal Astronomical Society*, 347, 471
- Petit, J.-M., Kavelaars, J. J., Gladman, B., & Loredó, T. 2008, in *The Solar System Beyond Neptune*, ed. M. A. Barucci, H. Boehnhardt, D. P. Cruikshank, A. Morbidelli, & R. Dotson (The University of Arizona Press), 71–87
- Petit, J.-M., Kavelaars, J. J., Gladman, B. J., et al. 2011, *The Astronomical Journal*, 142, 131
- Romanishin, W., Tegler, S. C., & Consolmagno, G. J. 2010, *The Astronomical Journal*, 140, 29
- Shankman, C., Gladman, B. J., Kaib, N., Kavelaars, J. J., & Petit, J.-M. 2013, *The Astrophysical Journal Letters*, 764, L2
- Skrutskie, M. F., Cutri, R. M., Stiening, R., et al. 2006, *The Astronomical Journal*, 131, 1163
- Souami, D., & Souchay, J. 2012, *Astronomy and Astrophysics*, 543, A133
- Stetson, P. B. 1987, *Astronomical Society of the Pacific*, 99, 191
- Tange, O. 2011, ;login: *The USENIX Magazine*, 36, 42
- The Astropy Collaboration, Robitaille, T. P., Tollerud, E. J., et al. 2013, *Astronomy and Astrophysics*, 558, A33
- Trujillo, C. 2000, *Minor Bodies in the Outer Solar System: Proceedings of the ESO Workshop Held at Garching*, 109
- Trujillo, C. A., Jewitt, D. C., & Luu, J. X. 2001, *The Astronomical Journal*, 122, 457
- Volk, K., Murray-Clay, R., Gladman, B., et al. submitted, 2015, *Astrophysical Journal*

Zacharias, N., Finch, C. T., Girard, T. M., et al. 2013, *The Astronomical Journal*, 145, 44